Inorg. Chem. **2005**, *44*, 5304–5321

Single-Molecule Magnets: Structural Characterization, Magnetic Properties, and ^{19}F NMR Spectroscopy of a Mn_{12} Family Spanning Three Oxidation Levels

Nicole E. Chakov,[†] Mònica Soler,[†] Wolfgang Wernsdorfer,[‡] Khalil A. Abboud,[†] and George Christou*[,†]

Department of Chemistry, University of Florida, Gainesville, Florida 32611-7200, and Laboratoire Louis Néel-CNRS, BP 166, 25 Avenue des Martyrs, 38042 Grenoble, Cedex 9, France

Received March 14, 2005

The syntheses, crystal structures, and magnetic properties of $[Mn_{12}O_{12}(O_2CC_6F_5)_{16}(H_2O)_4]$ (**2**), $(NMe_4)[Mn_{12}O_{12}(O_2CC_6F_5)_{16}(H_2O)_4]$ (**3**), and $(NMe_4)_2[Mn_{12}O_{12}(O_2CC_6F_5)_{16}(H_2O)_4]$ (**4**) are reported. Complex **2** displays quasi-reversible redox couples when examined by cyclic voltammetry in CH_2Cl_2: one-electron reductions are observed at 0.64 and 0.30 V vs ferrocene. The reaction of complex **2** with 1 and 2 equiv of NMe_4I yields the one- and two-electron reduced analogues, **3** and **4**, respectively. Complexes **2**·$3CH_2Cl_2$, **3**·$4.5CH_2Cl_2$·$^1/_2H_2O$, and **4**·$6C_7H_8$ crystallize in the triclinic $P\bar{1}$, monoclinic $P2/c$, and monoclinic $C2/c$ space groups, respectively. The molecular structures are all very similar, consisting of a central $[Mn^{IV}O_4]$ cubane surrounded by a nonplanar alternating ring of eight Mn and eight μ_3-O^{2-} ions. Peripheral ligation is provided by 16 bridging $C_6F_5CO_2^-$ and 4 H_2O ligands. Bond valence sum calculations establish that the added electrons in **3** and **4** are localized on former Mn^{III} ions giving trapped-valence $Mn^{IV}_4Mn^{III}_7Mn^{II}$ and $Mn^{IV}_4Mn^{III}_6Mn^{II}_2$ anions, respectively. ^{19}F NMR spectroscopy in CD_2Cl_2 shows retention of the solid-state structure upon dissolution and detrapping of the added electrons in **3** and **4** among the outer ring of Mn ions on the ^{19}F NMR time scale. DC studies on dried microcrystalline samples of **2**, **3**, and **4**·$2.5C_7H_8$ restrained in eicosane in the 1.80–10.0 K and 1–70 kG ranges were fit to give $S = 10$, $D = -0.40$ cm^{-1}, $g = 1.87$, $|D|/g = 0.21$ cm^{-1} for **2**, $S = 19/2$, $D = -0.34$ cm^{-1}, $g = 2.04$, $|D|/g = 0.17$ cm^{-1} for **3**, and $S = 10$, $D = -0.29$ cm^{-1}, $g = 2.05$, $|D|/g = 0.14$ cm^{-1} for **4**, where D is the axial zero-field splitting parameter. The clusters exhibit out-of-phase AC susceptibility signals (χ_M'') indicative of slow magnetization relaxation in the 6–8 K range for **2**, 4–6 K range for **3**, and 2–4 K range for **4**; the shift to lower temperatures reflects the decreasing magnetic anisotropy upon successive reduction and, hence, the decreasing energy barrier to magnetization relaxation. Relaxation rate vs T data obtained from χ_M'' vs AC oscillation frequency studies down to 1.8 K were combined with rate vs T data from DC magnetization decay vs time measurements at lower temperatures to generate an Arrhenius plot from which the effective barrier (U_{eff}) to magnetization reversal was obtained; the U_{eff} values are 59 K for **2**, 49 and 21 K for the slower- and faster-relaxing species of **3**, respectively, and 25 K for **4**. Hysteresis loops obtained from single-crystal magnetization vs DC field scans are typical of single-molecule magnets with the coercivities increasing with decreasing T and increasing field sweep rate and containing steps caused by the quantum tunneling of magnetization (QTM). The step separations gave $|D|/g$ values of 0.22 cm^{-1} for **2**, 0.15 and 0.042 cm^{-1} for the slower- and faster-relaxing species of **3**, and 0.15 cm^{-1} for **4**.

Introduction

Slow magnetization relaxation in molecules at low temperatures was first recognized in 1993 for $[Mn_{12}O_{12}(O_2CMe)_{16}(H_2O)_4]$·$2MeCO_2H$·$4H_2O$ (**1**).[1,2] This led to the birth of the new area of single-molecule magnets (SMMs), molecules that function as single-domain magnetic particles.[2−5] Such molecules have potential applications in a variety of areas, such as high-density information storage at the molecular level, whereby each bit of digital information is stored as the magnetization orientation of an individual

* To whom correspondence should be addressed. E-mail: christou@chem.ufl.edu.
[†] University of Florida.
[‡] Laboratoire Louis Néel.

(1) Sessoli, R.; Gatteschi, D.; Caneschi, A.; Novak, M. A. *Nature* **1993**, *365*, 141.

10.1021/ic050379w CCC: $30.25
Published on Web 06/30/2005

molecule.[6,7] Close examination of the hysteresis loops of **1** revealed a predicted quantum phenomenon that had never before been observed with certainty, quantum tunneling of magnetization (QTM),[8,9] prompting an explosion of research involving single-molecule magnetism in the physics area.[10] Molecules of **1** are of nanoscale dimensions, ~ 1.5 nm in diameter. Hence, they represent the point at which the classical and quantum worlds meet because they are macroscopic entities which display quantum effects.[7,8,11−13] One consequence of their QTM is that SMMs can also potentially function as qubits in quantum computers.[14]

In recent years, there has been a rapid increase in the number of molecules which have been found to behave as SMMs. Complexes of varying nuclearity, topology, and peripheral ligation have been prepared through the use of various transition metals. These include V,[15] Co,[16] Fe,[17] Ni,[18] and particularly, Mn.[19−24] However, although several new SMMs have been isolated and characterized, the highest temperature at which the reversal of magnetization is frozen (i.e., the blocking temperature, T_B) is still only ~3 K, the same as that which is exhibited by complex **1**.

The properties of a SMM that give rise to a significant energy barrier for magnetization reversal comprise a large ground-state spin, *S*, and a large negative (Ising-type) magnetic anisotropy as gauged by the zero-field splitting parameter, *D*.[1,2,3,25] Efforts are currently being concentrated on gaining a thorough understanding of how the structure of a molecule determines both *S* and *D* so that new SMMs with increased blocking temperatures can be designed. Hence, the study of the effects of the chemical variations of a molecule, the physical variations of a molecule, or both is extremely useful. Mn_{12} complexes have been modified in a number of ways,[22−24] and their resulting magnetic properties have been measured to gauge the effect of the changes on the behavior. One of the most informative changes made to this system was the preparation and isolation of the one-electron reduced Mn_{12} species, $(PPh_4)[Mn_{12}O_{12}(O_2CEt)$-

(2) (a) Sessoli, R.; Tsai, H.-L.; Schake, A. R.; Wang, S.; Vincent, J. B.; Folting, K.; Gatteschi, D.; Christou, G.; Hendrickson, D. N. *J. Am. Chem. Soc.* **1993**, *115*, 1804. (b) Aubin, S. M. J.; Wemple, M. W.; Adams, D. M.; Tsai, H.-L.; Christou, G.; Hendrickson, D. N. *J. Am. Chem. Soc.* **1996**, *118*, 7746.

(3) Christou, G.; Gatteschi, D.; Hendrickson, D. N.; Sessoli, R. *MRS Bull.* **2000**, *25*, 66.

(4) Barra, A.-L.; Debrunner, P.; Gatteschi, D.; Schultz, Ch. E.; Sessoli, R. *Europhys. Lett.* **1996**, *35*, 133.

(5) (a) Brockman, J. T.; Abboud, K. A.; Hendrickson, D. N.; Christou, G. *Polyhedron* **2003**, *22*, 1765. (b) Chakov, N. E.; Wernsdorfer, W.; Abboud, K. A.; Christou, G. *Inorg. Chem.* **2004**, *43*, 5919. (c) Mishra, A.; Wernsdorfer, W.; Abboud, K. A.; Christou, G. *J. Am. Chem. Soc.* **2004**, *126*, 15648. (d) Miyasaka, H.; Clérac, R.; Wernsdorfer, W.; Lecren, L.; Bonhomme, C.; Sugiura, K.; Yamashita, M. *Angew. Chem., Int. Ed.* **2004**, *43*, 2801. (e) Rajaraman, G.; Murugesu, M.; Sañudo, E. C.; Soler, M.; Wernsdorfer, W.; Helliwell, M.; Muryn, C.; Raftery, J.; Teat, S. J.; Christou, G.; Brechin, E. K. *J. Am. Chem. Soc.* **2004**, *126*, 15445. (f) Murugesu, M.; Raftery, J.; Wernsdorfer, W.; Christou, G.; Brechin, E. K. *Inorg. Chem.* **2004**, *43*, 4203. (g) Tasiopoulos, A. J.; Vinslava, A.; Wernsdorfer, W.; Abboud, K. A.; Christou, G. *Angew. Chem., Int. Ed.* **2004**, *43*, 2117. (h) Murugesu, M.; Wernsdorfer, W.; Abboud, K. A.; Christou, G. *Angew. Chem., Int. Ed.* **2005**, *44*, 892. (i) Foguet-Albiol, D.; O'Brien, T. A.; Wernsdorfer, W.; Moulton, B.; Zaworotko, M. J.; Abboud, K. A.; Christou, G. *Angew. Chem., Int. Ed.* **2005**, *44*, 897.

(6) Awschalom, D. D.; DiVincenzo, D. P. *Phys. Today* **1995**, *48*, 43.

(7) Caneschi, A.; Gatteschi, D.; Sangregorio, C.; Sessoli, R.; Sorace, L.; Cornia, A.; Novak, M. A.; Paulsen, C.; Wernsdorfer, W. *J. Magn. Magn. Mater.* **1999**, *200*, 182.

(8) Thomas, L.; Lionti, F.; Ballou, R.; Gatteschi, D.; Sessoli, R.; Barbara, B. *Nature* **1996**, *383*, 145.

(9) (a) Hendrickson, D. N.; Christou, G.; Ishimoto, H.; Yoo, J.; Brechin, E. K.; Yamaguchi, A.; Rumberger, E. M.; Aubin, S. M. J.; Sun, Z.; Aromí, G. *Polyhedron* **2001**, *20*, 1479. (b) Aubin, S. M. J.; Ruiz, D.; Rumberger, E.; Sun, Z.; Albela, B.; Wemple, M. W.; Dilley, N. R.; Ribas, J.; Maple, M. B.; Christou, G.; Hendrickson, D. N. *Mol. Cryst. Liq. Cryst.* **1999**, *335*, 371.

(10) (a) Hill, S.; Edwards, R. S.; Aliaga-Alcalde, N.; Christou, G. *Science* **2003**, *302*, 1015. (b) Wernsdorfer, W.; Soler, M.; Christou, G.; Hendrickson, D. N. *J. Appl. Phys.* **2002**, *91*, 7164.

(11) Wernsdorfer, W.; Aliaga-Alcalde, N.; Hendrickson, D. N.; Christou, G. *Nature* **2002**, *416*, 406.

(12) Wernsdorfer, W.; Sessoli, R. *Science* **1999**, *284*, 133.

(13) (a) Friedman, J. R.; Sarachik, M. P. *Phys. Rev. Lett.* **1996**, *76*, 3830. (b) Tejada, J.; Ziolo, R. F.; Zhang, X. X. *Chem. Mater.* **1996**, *8*, 1784.

(14) Leuenberger, M. N.; Loss, D. *Nature* **2001**, *410*, 789.

(15) Sun, Z.; Grant, C. M.; Castro, S. L.; Hendrickson, D. N.; Christou, G. *Chem. Commun.* **1998**, *6*, 721.

(16) Yang, E.-C.; Hendrickson, D. N.; Wernsdorfer, W.; Nakano, M.; Zakharov, L. N.; Sommer, R. D.; Rheingold, A. L.; Ledezma-Gairaud, M.; Christou, G. *J. Appl. Phys.* **1991**, *91*, 7382.

(17) (a) Sangregorio, C.; Ohm, T.; Paulsen, C.; Sessoli, R.; Gatteschi, D. *Phys. Rev. Lett.* **1997**, *78*, 4645. (b) Barra, A. L.; Caneschi, A.; Cornia, A.; Fabrizi de Biani, F.; Gatteschi, D.; Sangregorio, C.; Sessoli, R.; Sorace, L. *J. Am. Chem. Soc.* **1999**, *121*, 5302. (c) Goodwin, J. C.; Sessoli, R.; Gatteschi, D.; Wernsdorfer, W.; Powell, A. K.; Heath, S. L. *J. Chem. Soc., Dalton Trans.* **2000**, *12*, 1835. (d) Oshio, H.; Hoshino, N.; Ito, T. *J. Am. Chem. Soc.* **2000**, *122*, 12602. (e) Benelli, C.; Cano, J.; Journaux, Y.; Sessoli, R.; Solan, G. A.; Winpenny, R. E. P. *Inorg. Chem.* **2001**, *40*, 188. (f) Jones, L. F.; Brechin, E. K.; Collison, D.; Helliwell, M.; Mallah, T.; Piligkos, S.; Rajaraman, G.; Wernsdorfer, W. *Inorg. Chem.* **2003**, *42*, 6601. (g) Boudalis, A. K.; Donnadieu, B.; Nastopoulos, V.; Clemente-Juan, J. M.; Mari, A.; Sanakis, Y.; Tuchagues, J.-P.; Perlepes, S. P. *Angew. Chem., Int. Ed.* **2004**, *43*, 2266. (h) Moragues-Cánovas, M.; Rivière, É.; Ricard, L.; Paulsen, C.; Wernsdorfer, W.; Rajaraman, G.; Brechin, E. K.; Mallah, T. *Adv. Mater.* **2004**, *16*, 1101.

(18) (a) Nakano, M.; Matsubayashi, G.-E.; Muramatsu, T.; Kobayashi, T. C.; Amaya, K.; Yoo, J.; Christou, G.; Hendrickson, D. N. *Mol. Cryst. Liq. Cryst.* **2002**, *376*, 405. (b) Cadiou, C.; Murrie, M.; Paulsen, C.; Villar, V.; Wernsdorfer, W.; Winpenny, R. E. P. *Chem. Commun.* **2002**, *24*, 2666. (c) Ochsenbein, S. T.; Murrie, M.; Rusanov, E.; Stoeckli-Evans, H.; Sekine, C.; Güdel, H. U. *Inorg. Chem.* **2002**, *41*, 5133. (d) Yang, E.-C.; Wernsdorfer, W.; Hill, S.; Edwards, R. S.; Nakano, M.; Maccagnano, S.; Zakharov, L. N.; Rheingold, A. L.; Christou, G.; Hendrickson, D. N. *Polyhedron* **2003**, *22*, 1727.

(19) (a) Brechin, E. K.; Yoo, J.; Nakano, M.; Huffman, J. C.; Hendrickson, D. N.; Christou, G. *Chem. Commun.* **1999**, *9*, 783. (b) Yoo, J.; Brechin, E. K.; Yamaguchi, A.; Nakano, M.; Huffman, J. C.; Maniero, A. L.; Brunel, L.-C.; Awaga, K.; Ishimoto, H.; Christou, G.; Hendrickson, D. N. *Inorg. Chem.* **2000**, *39*, 3615. (c) Boskovic, C.; Wernsdorfer, W.; Folting, K.; Huffman, J. C.; Hendrickson, D. N.; Christou, G. *Inorg. Chem.* **2002**, *41*, 5107. (d) Boskovic, C.; Brechin, E. K.; Streib, W. E.; Folting, K.; Bollinger, J. C.; Hendrickson, D. N.; Christou, G. *J. Am. Chem. Soc.* **2002**, *124*, 3725. (e) Brechin, E. K.; Soler, M.; Davidson, J.; Hendrickson, D. N.; Parsons, S.; Christou, G. *Chem. Commun.* **2002**, *19*, 2252. (f) Price, D. J.; Batten, S. R.; Moubaraki, B.; Murray, K. S. *Chem. Commun.* **2002**, *7*, 762. (g) Tasiopoulos, A. J.; Wernsdorfer, W.; Moulton, B.; Zaworotko, M. J.; Christou, G. *J. Am. Chem. Soc.* **2003**, *125*, 15274. (h) Boskovic, C.; Bircher, R.; Tregenna-Piggott, P. L. W.; Güdel, H. U.; Paulsen, C.; Wernsdorfer, W.; Barra, A.-L.; Khatsko, E.; Neels, A.; Stoeckli-Evans, H. *J. Am. Chem. Soc.* **2003**, *125*, 14046. (i) Yang, E.-C.; Harden, N.; Wernsdorfer, W.; Zakharov, L.; Brechin, E. K.; Rheingold, A. L.; Christou, G.; Hendrickson, D. N. *Polyhedron* **2003**, *22*, 1857. (j) Murugesu, M.; Habrych, M.; Wernsdorfer, W.; Abboud, K. A.; Christou, G. *J. Am. Chem. Soc.* **2004**, *126*, 4766. (k) Tasiopoulos, A. J.; Wernsdorfer, W.; Abboud, K. A.; Christou, G. *Angew. Chem., Int. Ed.* **2004**, *43*, 6338. (l) King, P.; Wernsdorfer, W.; Abboud, K. A.; Christou, G. *Inorg. Chem.* **2004**, *43*, 7315. (m) Wittick, L. M.; Murray, K. S.; Moubaraki, B.; Batten, S. R.; Spiccia, L.; Berry, K. J. *J. Chem. Soc., Dalton Trans.* **2004**, *7*, 1003.

(20) (a) Soler, M.; Wernsdorfer, W.; Folting, K.; Pink, M.; Christou, G. *J. Am. Chem. Soc.* **2004**, *126*, 2156. (b) Soler, M.; Rumberger, E.; Folting, K.; Hendrickson, D. N.; Christou, G. *Polyhedron* **2001**, *20*, 1365.

$(H_2O)_4]$.[22] This was subsequently followed by the isolation of the two-electron reduced species, $(PPh_4)_2[Mn_{12}O_{12}(O_2CCHCl_2)_{16}(H_2O)_4]$.[24] Both complexes behave as SMMs, albeit at slightly lower temperatures than the neutral Mn_{12} species. A complete study, including hysteresis measurements on single crystals, of a family of such Mn_{12} complexes in multiple oxidation states and identical ligation is currently lacking. This is the topic of the present paper.

We herein describe the syntheses, single crystal X-ray structures, and magnetic properties of a family of Mn_{12} clusters with identical peripheral ligation spanning three oxidation levels: $[Mn_{12}O_{12}(O_2CC_6F_5)_{16}(H_2O)_4]$ (**2**), $(NMe_4)[Mn_{12}O_{12}(O_2CC_6F_5)_{16}(H_2O)_4]$ (**3**), and $(NMe_4)_2[Mn_{12}O_{12}(O_2CC_6F_5)_{16}(H_2O)_4]$ (**4**). This family has also been studied by inelastic neutron scattering (INS) measurements on the deuterated versions, and these results have recently been published elsewhere.[26]

Experimental Section

Syntheses. All manipulations were performed under aerobic conditions using materials as received, except where otherwise noted. $[Mn_{12}O_{12}(O_2CMe)_{16}(H_2O)_4]\cdot 4H_2O\cdot 2MeCO_2H$ (**1**) was prepared as described elsewhere.[27]

$[Mn_{12}O_{12}(O_2CC_6F_5)_{16}(H_2O)_4]$ (2). A slurry of complex **1** (2.0 g, 0.97 mmol) in CH_2Cl_2 (50 cm^3) was treated with $HO_2CC_6F_5$ (3.7 g, 0.017 mol). The solution was stirred overnight, and the solvent was removed in vacuo. Toluene (20 cm^3) was added to the residue, and the solution was again evaporated to dryness. The addition and removal of toluene was repeated two more times. The remaining solid was redissolved in CH_2Cl_2 (50 cm^3) and treated again with $HO_2CC_6F_5$ (0.41 g, 1.9 mmol). After 12 h, three more cycles of addition and removal of toluene were performed. The residue was redissolved in CH_2Cl_2 (50 cm^3) and filtered. An equal volume of heptane was added and the solution was allowed to stand undisturbed at room temperature for 4 days. The resulting black crystals were collected by filtration, washed with heptane, and dried in vacuo. Yield: 91%. Anal. Calcd (found) for $\mathbf{2}\cdot HO_2CC_6F_5$: C, 31.86% (31.90%); H, 0.21% (0.38%). A crystallography sample was grown slowly from CH_2Cl_2/heptane and maintained in the mother liquor to avoid solvent loss. Selected IR data (KBr, cm^{-1}): ν 1699 (w), 1604 (vs), 1552 (s), 1507 (s), 1471 (m), 1417 (vs), 1351 (s), 1302 (m), 1231 (s), 1152 (vs), 1091 (m), 1015 (m), 857 (s), 797 (w), 778 (vs), 692 (m), 667 (m), 632 (s, br), 549 (m), 520 (m), 500 (m), 441 (w), 418 (w).

$(NMe_4)[Mn_{12}O_{12}(O_2CC_6F_5)_{16}(H_2O)_4]$ (3). Solid NMe_4I (0.047 g, 0.23 mmol) was added to a stirred dark brown solution of complex **2** (1.0 g, 0.23 mmol) in MeCN (70 cm^3). The solution was stirred overnight with no noticeable color change. Hexanes (25 cm^3) were added to the reaction solution to facilitate the extraction of I_2; the layer of hexanes was removed, and the MeCN layer was evaporated to dryness. The residue was redissolved in MeCN (50 cm^3), and hexanes (25 cm^3) were again added to extract further I_2. The layers were separated, and the MeCN solution evaporated to dryness. This process was repeated six more times to complete the removal of I_2. The residue was dissolved in CH_2Cl_2 (50 cm^3) and filtered. An equal volume of heptane was added, and the solution was allowed to stand undisturbed for 4 days. The resulting black microcrystalline product was recrystallized twice more, filtered, washed with heptane, and dried in vacuo. Yield: 74%. Anal. Calcd (found) for **3**: C, 31.85% (32.00%); H, 0.46% (0.47%); N, 0.32% (0.33%). X-ray quality crystals were grown slowly from CH_2Cl_2/heptane and maintained in the mother liquor to avoid solvent loss. Selected IR data (KBr, cm^{-1}): ν 1649 (s), 1604 (s), 1557 (m), 1522 (s), 1492 (vs), 1417 (vs), 1387 (vs), 1294 (m), 1116 (m), 996 (s), 948 (m), 936 (m), 823 (w), 758 (s), 746 (s), 708 (m), 653 (m), 608 (m), 583 (m), 560 (m), 525 (m), 505 (w), 455 (w), 420 (w).

$(NMe_4)_2[Mn_{12}O_{12}(O_2CC_6F_5)_{16}(H_2O)_4]$ (4). Solid NMe_4I (0.094 g, 0.47 mmol) was added to a stirred dark brown solution of complex **2** (1.0 g, 0.23 mmol) in MeCN (70 cm^3). The solution was stirred overnight with no noticeable color change. Hexanes (25 cm^3) were added to the reaction solution to facilitate the extraction of I_2 as for **3**, and the separated MeCN solution was evaporated to dryness. The residue was redissolved in MeCN (50 cm^3); hexanes (25 cm^3) were again added, and the solution was evaporated to dryness. This process was repeated six more times to complete the removal of I_2. The residue was dissolved in CH_2Cl_2 (50 cm^3) and filtered. Crystals were obtained by addition of a mixture of heptane and toluene to the CH_2Cl_2 solution. The resulting black microcrystalline product was recrystallized twice, filtered, washed with heptane, and dried in vacuo. Yield: 70%. Anal. Calcd. (found) for **4**: C, 32.40% (32.39%); H, 0.73% (0.68%); N, 0.63% (0.63%). X-ray quality crystals were grown slowly from CH_2Cl_2/heptane−toluene (1:1) and maintained in the mother liquor to avoid solvent loss. Selected IR data (KBr, cm^{-1}): ν 1616 (vs), 1523 (vs), 1489 (vs), 1381 (vs), 1356 (s), 1291 (m), 1105 (m), 993 (s), 950 (m), 930 (m), 832 (w), 764 (s), 752 (s), 738 (s), 583 (s, br), 508 (m).

X-ray Crystallography. Data were collected using a Siemens SMART PLATFORM equipped with a CCD area detector and a graphite monochromator utilizing Mo Kα radiation (λ = 0.71073 Å). Suitable single crystals of $\mathbf{2}\cdot 3CH_2Cl_2$, $\mathbf{3}\cdot 4.5CH_2Cl_2\cdot {}^1/_2H_2O$, and $\mathbf{4}\cdot 6C_7H_8$ were attached to glass fibers using silicone grease and transferred to the goniostat where they were cooled to

(21) (a) Brechin, E. K.; Boskovic, C.; Wernsdorfer, W.; Yoo, J.; Yamaguchi, A.; Sañudo, E. C.; Concolino, T. R.; Rheingold, A. L.; Ishimoto, H.; Hendrickson, D. N.; Christou, G. *J. Am. Chem. Soc.* **2002**, *124*, 9710. (b) Sañudo, E. C.; Brechin, E. K.; Boskovic, C.; Wernsdorfer, W.; Yoo, J.; Yamaguchi, A.; Concolino, T. R.; Abboud, K. A.; Rheingold, A. L.; Ishimoto, H.; Hendrickson, D. N.; Christou, G. *Polyhedron* **2003**, *22*, 2267. (c) Brechin, E. K.; Sañudo, E. C.; Wernsdorfer, W.; Boskovic, C.; Yoo, J.; Hendrickson, D. N.; Yamaguchi, A.; Ishimoto, H.; Concolino, T. R.; Rheingold, A. L.; Christou, G. *Inorg. Chem.* **2005**, *44*, 502.

(22) Eppley, H. J.; Tsai, H.-L.; de Vries, N.; Folting, K.; Christou, G.; Hendrickson, D. N. *J. Am. Chem. Soc.* **1995**, *117*, 301.

(23) (a) Eppley, H. J.; Christou, G.; Law, N. A.; Pecoraro, V. L. *Inorg. Synth.* **2002**, *33*, 61. (b) Soler, M.; Artus, P.; Folting, K.; Huffman, J. C.; Hendrickson, D. N.; Christou, G. *Inorg. Chem.* **2001**, *40*, 4902. (c) Aubin, S. M. J.; Sun, Z.; Pardi, L.; Krzystek, J.; Folting, K.; Brunel, L.-C.; Rheingold, A. L.; Christou, G.; Hendrickson, D. N. *Inorg. Chem.* **1999**, *38*, 5329. (d) Schake, A. R.; Tsai, H.-L.; Webb, R. J.; Folting, K.; Christou, G.; Hendrickson, D. N. *Inorg. Chem.* **1994**, *33*, 6020. (e) Li, J.-Y.; Xu, H.; Zou, J.-Z.; Xu, Z.; You, X.-Z.; Yu, K.-P. *Polyhedron* **1996**, *15*, 3325. (f) Artus, P.; Boskovic, C.; Yoo, J.; Streib, W. E.; Brunel, L.-C.; Hendrickson, D. N.; Christou, G. *Inorg. Chem.* **2001**, *40*, 4199. (g) Boskovic, C.; Pink, M.; Huffman, J. C.; Hendrickson, D. N.; Christou, G. *J. Am. Chem. Soc.* **2001**, *123*, 9914. (h) Chakov, N. E.; Wernsdorfer, W.; Abboud, K. A.; Hendrickson, D. N.; Christou, G. *J. Chem. Soc., Dalton Trans.* **2003**, *11*, 2243. (i) Kuroda-Sowa, T.; Fukuda, S.; Miyoshi, S.; Maekawa, M.; Munakata, M.; Miyasaka, H.; Yamashita, M. *Chem. Lett.* **2002,** *31*, 682. (j) Artus, P.; Christou, G. manuscript in preparation.

(24) Soler, M.; Wernsdorfer, W.; Abboud, K. A.; Huffman, J. C.; Davidson, E. R.; Hendrickson, D. N.; Christou, G. *J. Am. Chem. Soc.* **2003**, *125*, 3576.

(25) Caneschi, A.; Gatteschi, D.; Sessoli, R. *J. Am. Chem. Soc.* **1991**, *113*, 5873.

(26) Basler, R.; Sieber, A.; Chaboussant, G.; Güdel, H. U.; Chakov, N. E.; Soler, M.; Christou, G.; Desmedt, A.; Lechner, R. *Inorg. Chem.* **2005**, *44*, 649.

(27) Lis, T. *Acta Crystallogr.* **1980**, *B36*, 2042.

Table 1. Crystallographic Data for Complexes **2**·$3CH_2Cl_2$, **3**·$4.5CH_2Cl_2$·$^1/_2H_2O$, and **4**·$6C_7H_8$

	2	**3**	**4**
formula[a]	$C_{115}H_{14}Cl_6Mn_{12}F_{80}O_{48}$	$C_{120.5}H_{30}Cl_9Mn_{12}N_1F_{80}O_{48.5}$	$C_{162}H_{80}Mn_{12}N_2F_{80}O_{48}$
fw (g mol^{-1})	4555.19	4765.74	5001.53
space group	$P\bar{1}$	$P2/c$	$C2/c$
a (Å)	18.519(4)	33.6633(2)	21.7892(15)
b (Å)	18.895(4)	17.3311(9)	27.0937(19)
c (Å)	26.169(5)	27.2564(2)	31.623(2)
α (deg)	70.073(2)	90	90
β (deg)	72.616(2)	94.2090(2)	91.640(2)
γ (deg)	73.364(3)	90	90
V (Å^3)	8040(3)	15859.1(2)	18661(2)
Z	2	4	4
T (°C)	−80(2)	−80(2)	−100(2)
radiation (Å)[b]	0.71073	0.71073	0.71073
ρ_{calc} (g cm^{-3})	1.882	1.996	1.780
μ (cm^{-1})	11.77	12.48	9.40
R1 (wR2) (%)[c,d]	8.80 (21.79)	5.34 (13.25)	5.81 (14.31)

[a] Including solvent molecules. [b] Graphite monochromator. [c] $R1 = \sum||F_o| - |F_c||/\sum|F_o|$. [d] $wR2 = \{\sum[w(F_o^2 - F_c^2)^2]/\sum[wF_o^2)^2]\}^{1/2}$ where $S = \{\sum[w(F_o^2 - F_c^2)^2]/(n\text{-}p)\}^{1/2}$, $w = 1/[\sigma^2(F_o^2) + (mp)^2 + np]$, $p = [\max(F_o^2, 0) + 2F_c^2]/3$, and m and n are constants.

−80 °C (**2** and **3**) and −100 °C (**4**) for characterization and data collection. Each structure was solved by direct methods (SHELXTL)[28] and standard Fourier techniques, and was refined using full-matrix least-squares methods. All non-hydrogen atoms were refined anisotropically. Cell parameters were refined using up to 8192 reflections. For each complex, a full sphere of data (1850 frames) was collected using the ω-scan method (0.3° frame width). The first 50 frames were remeasured at the end of data collection to monitor instrument and crystal stability (maximum correction on I was < 1%). Absorption corrections by integration were applied on the basis of measured indexed crystal faces.

A preliminary search of the reciprocal space for **2**·$3CH_2Cl_2$ revealed a set of reflections with no symmetry and no systematic absences. An initial choice of the centrosymmetric space group $P\bar{1}$ was subsequently confirmed by the successful solution of the structure. The asymmetric unit contains the Mn_{12} molecule and three disordered CH_2Cl_2 molecules of crystallization. The solvent molecules were significantly disordered and could not be modeled properly. Hence, the program SQUEEZE,[29] a part of the PLATON[30] package of crystallographic software, was used to calculate the solvent disorder area and remove its contribution to the overall intensity data. The pentafluorophenyl rings in two of the $C_6F_5CO_2^-$ ligands, C(9)−C(14) and C(16)−C(21), were disordered over two positions, whose site occupancy factors were dependently refined to 70:30% and 54:46%, respectively. Hydrogen atoms of the water ligands were not located and therefore not included in the final cycle of refinement. A total of 2266 parameters were refined in the final cycle of refinement using 10424 reflections with $I > 2\sigma(I)$ to yield R1 and wR2 values of 8.80% and 21.79%, respectively. The final difference Fourier map was essentially featureless, the largest peak being 1.211 e Å^{-3} and the deepest hole being −0.702 e Å^{-3}.

For complex **3**·$4.5CH_2Cl_2$·$^1/_2H_2O$, an initial survey of a portion of reciprocal space located a set of reflections with a monoclinic lattice. Analysis of the full data set revealed that the space group was $P2/c$. The asymmetric unit contains the Mn_{12} molecule, two one-half NMe_4^+ cations, 4.5 CH_2Cl_2 molecules, and half of a water molecule of crystallization. Hydrogen atoms of the cations and solvent molecules were calculated in ideal positions and were refined with the use of a riding model. The hydrogen atoms of the four coordinated water molecules were located from a difference Fourier map and refined freely. A disorder was observed involving a water molecule [O(17)] and a pentafluorobenzoate ligand [O(21)−C(64)−O(18)]. Each was refined in two positions with their site occupancies being 77:23%. Atoms of the minor disorder position were refined with isotropic thermal parameters. A total of 2479 parameters were refined in the final cycle of refinement using 18144 reflections with $I > 2\sigma(I)$ to yield R1 and wR2 values of 5.34% and 13.25%, respectively. The final difference Fourier map was essentially featureless with the largest peak and deepest hole being 1.704 and −1.540 e Å^{-3}, respectively.

A preliminary search of the reciprocal space for **4**·$6C_7H_8$ revealed a set of reflections with a monoclinic lattice. An initial choice of the space group $C2/c$ was subsequently confirmed by the successful solution of the structure. The asymmetric unit contains half of the Mn_{12} molecule, two toluene molecules in general positions, two one-half toluene molecules, each of which is disordered over a center of inversion, and one NMe_4^+ cation. Hydrogen atoms were calculated in ideal positions and were refined with the use of a riding model. The pentafluorophenyl rings in two of the $C_6F_5CO_2^-$ ligands, C(16)−C(21) and C(51)−C(56), were disordered over two sites, whose site occupancy factors were dependently refined to 58:42% and 50:50%, respectively. A total of 1415 parameters were refined in the final cycle of refinement using 7055 reflections with $I > 2\sigma(I)$ to yield R1 and wR2 values of 5.81% and 14.31%, respectively. The final difference Fourier maps were reasonably clean, the maximum and minimum residual electron density being 0.933 and −0.620 e Å^{-3}, respectively.

The crystallographic data and structure refinement details are collected in Table 1.

Other Studies. Infrared spectra were recorded in the solid state (KBr pellets) on a Nicolet Nexus 670 FTIR spectrophotometer in the 400−4000 cm^{-1} range. Elemental analyses (C, H, and N) were performed at the in-house facilities of the University of Florida Chemistry Department. Electrochemical studies were performed under argon using a BAS model CV-50W voltammetric analyzer and a standard three-electrode assembly (glassy carbon working, Pt wire auxiliary, and Ag/Ag_3I_4 reference) with 0.1 M $NBu^n_4PF_6$ as supporting electrolyte. No IR compensation was employed. Quoted potentials are vs the ferrocene/ferrocenium couple, used as an internal standard. The scan rates for cyclic voltammetry (CV) and differential pulse voltammetry (DPV) were 100 and 20 mV/s, respectively. Distilled solvents were employed, and the concentrations of the complexes were approximately 1 mM. ^{19}F NMR spectra

(28) Sheldrick, G. M. *SHELXTL5*; Bruker-AXS:, Madison, Wisconsin, 1998.
(29) van der Sluis, P.; Spek, A. L. *Acta Crystallogr.* **1990**, *A46*, 194.
(30) Spek, A. L. *Acta Crystallogr.* **1990**, *A46*, 1.

were obtained at 282 MHz on a Varian VXR-300 spectrometer, using $CFCl_3$ as an internal standard. Variable-temperature DC magnetic susceptibility data down to 1.80 K were collected on a Quantum Design MPMS-XL SQUID magnetometer equipped with a 70 kG (7 T) DC magnet at the University of Florida. Samples were restrained in eicosane to prevent torquing. Pascal's constants were used to estimate the diamagnetic corrections, which were subtracted from the experimental susceptibility to give the molar magnetic susceptibility (χ_M). AC magnetic susceptibility data were collected on the same instrument employing a 3.5 G field oscillating at frequencies up to 1500 Hz. Low-temperature (<1.8 K) hysteresis loop and DC relaxation measurements were performed at Grenoble using an array of micro-SQUIDS.[31] The high sensitivity of this magnetometer allows the study of single crystals of SMMs of the order of 10−500 μm. The field can be applied in any direction by separately driving three orthogonal coils.

Results and Discussion

Syntheses. Employing the previously developed ligand substitution procedure, which involves the treatment of **1** with an excess of a carboxylic acid, pentafluorobenzoate ligands were introduced onto the Mn_{12} complex.[22,23a] The transformation of **1** into **2** is summarized in eq 1.

$$[Mn_{12}O_{12}(O_2CMe)_{16}(H_2O)_4] + 16C_6F_5CO_2H \rightarrow [Mn_{12}O_{12}(O_2CC_6F_5)_{16}(H_2O)_4] + 16MeCO_2H \quad (1)$$

The ligand substitution reaction is an equilibrium that favors the product side when the pK_a of the added acid is lower than that of acetic acid; the pK_a of $C_6F_5CO_2H$ is 1.48,[32] while that of $MeCO_2H$ is 4.76. A consequence of this considerable difference is that the fully substituted derivative can be obtained in high yield when only a slight excess of $C_6F_5CO_2H$ is used to treat complex **1**. In addition, acetic acid removal from the reaction system under low pressure as its toluene azeotrope (28/72%; bp 101 °C at atmospheric pressure) guarantees complete substitution.[23a]

The redox chemistry of a number of Mn_{12} derivatives has been thoroughly explored.[22,24] Cyclic voltammograms typically exhibit at least one quasi-reversible reduction wave and frequently a second quasi-reversible one as well. The reduction potentials are highly dependent on the electron-donating or electron-withdrawing nature of the carboxylate ligand (RCO_2^-). The first reduction potential occurs over a wide range, from 0.00 V for R = C_6H_4-*p*-OMe to 0.91 V for R = $CHCl_2$ (vs the Fc/Fc^+ couple).[22,24] In previous reports, it was shown that with the use of stoichiometric amounts of I^- as a reducing agent (the I^-/I_2 couple occurs at 0.21 V in CH_2Cl_2 vs Fc/Fc^+), both the one- and two-electron reduced Mn_{12} species could be generated in bulk in CH_2Cl_2. The isolation and structural characterization of both $(PPh_4)[Mn_{12}O_{12}(O_2CEt)_{16}(H_2O)_4]$ and $(PPh_4)_2[Mn_{12}O_{12}(O_2CCHCl_2)_{16}(H_2O)_4]$ as well as others have been described.[22,23c,24,33]

The cyclic voltammogram (CV) and differential pulse voltammogram (DPV) for complex **2** are shown in Figure 1. Two reduction processes are displayed at 0.64 and 0.30 V, each of which appears quasi-reversible. This reversibility was assessed on the basis of the usual electrochemical criteria, including CV peak separations, anodic/cathodic peak current ratio, DPV peak broadness, and proportionality of the peak current to the square root of the scan rate (υ). In the latter, a study of the scan rate dependence for the 0.64 and 0.30 V reduction processes showed a linear dependence of the peak current with $\upsilon^{1/2}$, indicating that the reductions are diffusion-controlled processes. As expected, the $E_{1/2}$ values are rather positive, in accordance with the strongly electron-withdrawing substituents in $C_6F_5CO_2^-$, and both the first and second reductions are consequently within the capability of the reducing agent, I^-.

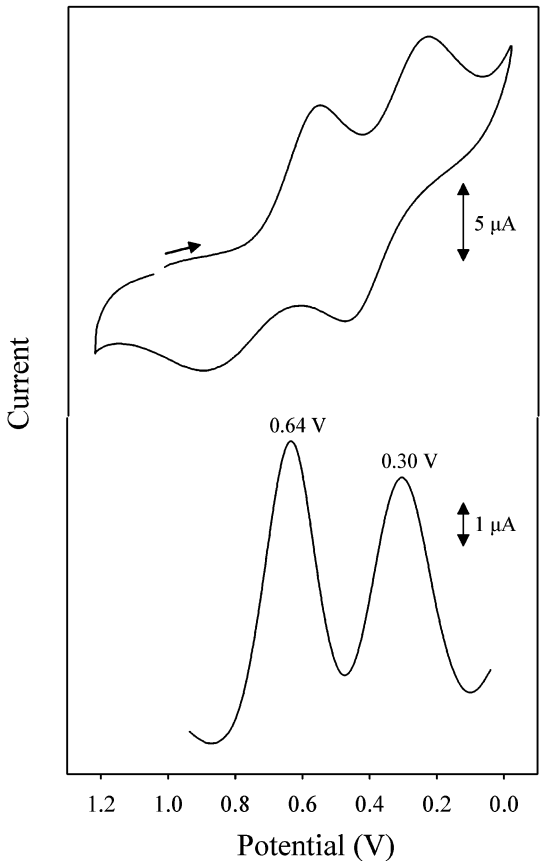

Figure 1. Cyclic voltammogram at 100 mV s^{-1} (top) and differential pulse voltammogram (bottom) for complex **2** in CH_2Cl_2 containing 0.1 M $NBu^n_4PF_6$ as the supporting electrolyte. The indicated potentials are given versus ferrocene as an internal standard.

Thus, $[Mn_{12}O_{12}(O_2CC_6F_5)_{16}(H_2O)_4]$ (**2**) was treated with 1 and 2 equiv of NMe_4I in MeCN; the formation of I_2 was confirmed by its extraction into a hexane phase. Removal of MeCN in vacuo and recrystallization of the residue from CH_2Cl_2 with heptane or heptane/toluene (1:1) gave black crystals of the desired one- and two-electron reduced complexes, **3** and **4**, in good yield (≥70%) and analytical

(31) Wernsdorfer, W. *Adv. Chem. Phys.* **2001**, *118*, 99.
(32) Strong, L. E.; Brummel, C. L.; Lindower, P. *J. Solution Chem.* **1987**, *16*, 105.
(33) (a) Tsai, H.-L.; Jwo, T.-Y.; Lee, G.-H.; Wang, Y. *Chem. Lett.* **2000**, *29*, 346. (b) Kuroda-Sowa, T.; Lam, M.; Rheingold, A. L.; Frommen, C.; Reiff, W. M.; Nakano, M.; Yoo, J.; Maniero, A. L.; Brunel, L.-C.; Christou, G.; Hendrickson, D. N. *Inorg. Chem.* **2001**, *40*, 6469. (c) Kuroda-Sowa, T.; Nogami, T.; Konaka, H.; Maekawa, M.; Munakata, M.; Miyasaka, H.; Yamashita, M. *Polyhedron* **2003**, *22*, 1795.

Table 2. Selected Bond Distances (Å) for Complex **2**[a]

Mn(1)−O(2)	1.874(8)	Mn(6)−O(3)	1.904(6)
Mn(1)−O(1)	1.915(7)	Mn(6)−O(10)	1.917(6)
Mn(1)−O(15)	1.933(9)	Mn(6)−O(27)	1.920(7)
Mn(1)−O(14)	1.958(10)	Mn(6)···Mn(7)	2.941(2)
Mn(1)−O(13)	2.184(8)	Mn(7)−O(12)	1.850(7)
Mn(1)−O(16)	2.207(8)	Mn(7)−O(11)	1.868(6)
Mn(1)···Mn(2)	2.779(2)	Mn(7)−O(4)	1.898(6)
Mn(2)−O(1)	1.864(7)	Mn(7)−O(10)	1.909(7)
Mn(2)−O(2)	1.864(6)	Mn(7)−O(28)	1.920(7)
Mn(2)−O(10)	1.905(6)	Mn(7)−O(9)	1.922(6)
Mn(2)−O(17)	1.914(7)	Mn(7)···Mn(8)	2.796(2)
Mn(2)−O(4)	1.920(7)	Mn(8)−O(11)	1.903(7)
Mn(2)−O(3)	1.926(6)	Mn(8)−O(31)	1.909(8)
Mn(2)···Mn(6)	2.814(2)	Mn(8)−O(12)	1.910(6)
Mn(2)···Mn(7)	2.840(2)	Mn(8)−O(30)	1.927(10)
Mn(2)···Mn(3)	2.962(2)	Mn(8)−O(29)	2.227(8)
Mn(3)−O(6)	1.874(7)	Mn(8)−O(32)	2.244(10)
Mn(3)−O(5)	1.880(6)	Mn(9)−O(8)	1.865(6)
Mn(3)−O(9)	1.906(6)	Mn(9)−O(1)	1.880(7)
Mn(3)−O(4)	1.907(6)	Mn(9)−O(35)	1.957(8)
Mn(3)−O(3)	1.927(6)	Mn(9)−O(34)	1.978(7)
Mn(3)−O(18)	1.931(6)	Mn(9)−O(36)	2.168(7)
Mn(3)···Mn(4)	2.795(2)	Mn(9)−O(33)	2.212(7)
Mn(3)···Mn(7)	2.813(2)	Mn(10)−O(5)	1.891(6)
Mn(3)···Mn(6)	2.834(2)	Mn(10)−O(7)	1.903(6)
Mn(4)−O(5)	1.876(7)	Mn(10)−O(39)	1.956(6)
Mn(4)−O(6)	1.913(6)	Mn(10)−O(38)	1.964(6)
Mn(4)−O(21)	1.926(8)	Mn(10)−O(37)	2.148(7)
Mn(4)−O(20)	1.960(6)	Mn(10)−O(40)	2.162(8)
Mn(4)−O(22)	2.161(7)	Mn(11)−O(11)	1.884(7)
Mn(4)−O(19)	2.195(7)	Mn(11)−O(46)	1.978(10)
Mn(5)−O(7)	1.874(7)	Mn(11)−O(2)	1.978(8)
Mn(5)−O(8)	1.909(6)	Mn(11)−O(48)	2.010(9)
Mn(5)−O(25)	1.934(7)	Mn(11)−O(45)	2.015(8)
Mn(5)−O(24)	1.947(7)	Mn(11)−O(47)	2.053(10)
Mn(5)−O(26)	2.161(7)	Mn(12)−O(12)	1.869(7)
Mn(5)−O(23)	2.172(7)	Mn(12)−O(6)	1.875(7)
Mn(5)···Mn(6)	2.785(2)	Mn(12)−O(42)	1.963(9)
Mn(6)−O(8)	1.869(7)	Mn(12)−O(43)	1.974(8)
Mn(6)−O(7)	1.894(6)	Mn(12)−O(44)	2.201(8)
Mn(6)−O(9)	1.895(7)	Mn(12)−O(41)	2.211(8)

[a] Full listings are in the Supporting Information.

purity. The transformation of **2** into both **3** and **4** is summarized in eq 2, where $n = 1$ or 2.

$$[Mn_{12}O_{12}(O_2CC_6F_5)_{16}(H_2O)_4] + nNMe_4I \rightarrow (NMe_4)_n[Mn_{12}O_{12}(O_2CC_6F_5)_{16}(H_2O)_4] + {}^n/_2I_2 \quad (2)$$

Description of Structures. Labeled ORTEP[34] plots, in the PovRay format, of complexes **2**, **3**, and **4** are presented in Figures 2, 3, and 5, together with stereoviews. Selected bond distances are listed in Tables 2, 3, and 4, respectively.

Complex **2**·$3CH_2Cl_2$ crystallizes in the triclinic space group $P\bar{1}$ (Figure 2). The structure consists of a central $[Mn^{IV}_4O_4]$ cubane core surrounded by a nonplanar ring of eight Mn^{III} ions which are bridged and connected to the cubane by eight μ_3-O^{2-} ions. The eight Mn^{III} ions separate into two groups of four Mn^{III} ions each. In the first group, each Mn^{III} ion is coordinated to a single Mn^{IV} ion via two oxide bridges [Mn(1), Mn(4), Mn(5), Mn(8)], while in the second group each Mn^{III} ion is coordinated to two Mn^{IV} ions via two oxide bridges [Mn(9), Mn(10), Mn(11), Mn(12)].[35] Peripheral ligation is provided by sixteen bridging $C_6F_5CO_2^-$ ligands

Table 3. Selected Bond Distances (Å) for Complex **3**[a]

Mn(1)−O(1)	1.874(3)	Mn(6)−O(7)	1.915(3)
Mn(1)−O(5)	1.882(3)	Mn(6)−O(24)	1.992(4)
Mn(1)−O(6)	1.890(3)	Mn(6)−O(20)	2.031(4)
Mn(1)−O(2)	1.907(3)	Mn(6)−O(22)	2.069(4)
Mn(1)−O(4)	1.911(3)	Mn(6)−O(21)	2.072(4)
Mn(1)−O(14)	1.924(3)	Mn(7)−O(8)	1.856(3)
Mn(1)···Mn(4)	2.7972(9)	Mn(7)−O(7)	1.885(3)
Mn(1)···Mn(5)	2.8012(10)	Mn(7)−O(28)	1.947(3)
Mn(1)···Mn(2)	2.8253(10)	Mn(7)−O(25)	1.981(3)
Mn(1)···Mn(3)	2.9486(9)	Mn(7)−O(23)	2.199(3)
Mn(2)−O(8)	1.832(3)	Mn(7)−O(27)	2.236(4)
Mn(2)−O(7)	1.856(3)	Mn(8)−O(9)	2.080(3)
Mn(2)−O(2)	1.915(3)	Mn(8)−O(29)	2.135(3)
Mn(2)−O(26)	1.927(3)	Mn(8)−O(8)	2.153(3)
Mn(2)−O(3)	1.943(3)	Mn(8)−O(30)	2.164(3)
Mn(2)−O(1)	1.967(3)	Mn(8)−O(48)	2.179(4)
Mn(2)−Mn(7)	2.7454(10)	Mn(8)−O(47)	2.200(4)
Mn(2)···Mn(3)	2.8654(10)	Mn(9)−O(9)	1.842(3)
Mn(2)···Mn(4)	2.9575(9)	Mn(9)−O(10)	1.919(3)
Mn(3)−O(9)	1.818(3)	Mn(9)−O(31)	1.947(3)
Mn(3)−O(10)	1.878(3)	Mn(9)−O(36)	1.957(3)
Mn(3)−O(3)	1.903(3)	Mn(9)−O(32)	2.193(3)
Mn(3)−O(2)	1.944(3)	Mn(9)−O(34)	2.206(3)
Mn(3)−O(4)	1.945(3)	Mn(10)−O(10)	1.860(3)
Mn(3)−O(33)	1.951(3)	Mn(10)−O(11)	1.898(3)
Mn(3)···Mn(9)	2.7645(10)	Mn(10)−O(40)	1.947(3)
Mn(3)···Mn(4)	2.8284(9)	Mn(10)−O(37)	2.007(3)
Mn(4)−O(11)	1.875(3)	Mn(10)−O(38)	2.150(3)
Mn(4)−O(4)	1.884(3)	Mn(10)−O(35)	2.163(3)
Mn(4)−O(12)	1.903(3)	Mn(11)−O(11)	1.883(3)
Mn(4)−O(1)	1.905(3)	Mn(11)−O(12)	1.901(3)
Mn(4)−O(3)	1.916(3)	Mn(11)−O(42)	1.953(3)
Mn(4)−O(45)	1.945(3)	Mn(11)−O(41)	1.977(3)
Mn(4)···Mn(11)	2.7957(9)	Mn(11)−O(39)	2.164(3)
Mn(5)−O(5)	1.880(3)	Mn(11)−O(44)	2.179(3)
Mn(5)−O(6)	1.895(3)	Mn(12)−O(5)	1.868(3)
Mn(5)−O(19)	1.919(3)	Mn(12)−O(12)	1.881(3)
Mn(5)−O(16)	1.957(3)	Mn(12)−O(43)	1.948(3)
Mn(5)−O(18)	2.204(4)	Mn(12)−O(15)	1.971(3)
Mn(5)−O(13)	2.222(3)	Mn(12)−O(17)	2.207(4)
Mn(6)−O(6)	1.899(3)	Mn(12)−O(46)	2.221(4)

[a] Full listings are in the Supporting Information

Table 4. Selected Bond Distances (Å)for Complex **4**[a]

Mn(1)−O(4)	1.832(4)	Mn(3)−O(10)	1.949(4)
Mn(1)−O(3)	1.869(4)	Mn(3)−O(11)	2.197(4)
Mn(1)−O(2)	1.889(3)	Mn(3)−O(9)	2.268(4)
Mn(1)−O(1a)	1.921(3)	Mn(4)−O(6)	1.878(4)
Mn(1)−O(1)	1.945(4)	Mn(4)−O(3)	1.882(4)
Mn(1)−O(5)	1.947(3)	Mn(4)−O(14)	1.967(4)
Mn(1)···Mn(5)	2.7717(12)	Mn(4)−O(13)	1.979(4)
Mn(1)···Mn(2)	2.8206(12)	Mn(4)−O(15)	2.151(4)
Mn(1)···Mn(2a)	2.8582(12)	Mn(4)−O(12)	2.180(4)
Mn(1)···Mn(1a)	2.9588(17)	Mn(5)−O(4)	1.862(4)
Mn(2)−O(7)	1.830(4)	Mn(5)−O(3)	1.904(4)
Mn(2)−O(6)	1.877(4)	Mn(5)−O(17)	1.955(4)
Mn(2)−O(1)	1.893(3)	Mn(5)−O(18)	1.980(4)
Mn(2)−O(2a)	1.921(4)	Mn(5)−O(19)	2.171(4)
Mn(2)−O(8)	1.940(4)	Mn(5)−O(16)	2.193(4)
Mn(2)−O(2)	1.942(4)	Mn(6)−O(7a)	2.075(4)
Mn(2)···Mn(3)	2.7638(13)	Mn(6)−O(4)	2.117(4)
Mn(2)···Mn(1a)	2.8582(12)	Mn(6)−O(21)	2.126(5)
Mn(2)···Mn(2a)	2.9392(18)	Mn(6)−O(22)	2.139(5)
Mn(3)−O(7)	1.841(4)	Mn(6)−O(20)	2.219(4)
Mn(3)−O(6)	1.901(4)	Mn(6)−O(23)	2.281(4)
Mn(3)−O(24a)	1.944(5)		

[a] Full listings are in the Supporting Information

and four terminal H_2O molecules [O(33), O(36), O(41), O(44)], which are bound in a 2:2 fashion to two trans Mn^{III} ions, Mn(9) and Mn(12) (Figure 2). This disposition of two pairs of H_2O ligands has also been observed for $[Mn_{12}O_{12}$-

(34) Johnson, C. K.; Burnett, M. N. *ORTEP−III*; Report ORNL-6895, Oak Ridge National Laboratory: Oak Ridge, TN, 1996. (b) Farrugia, L. J. *J. Appl. Crystallogr.* **1997**, *30*, 565.

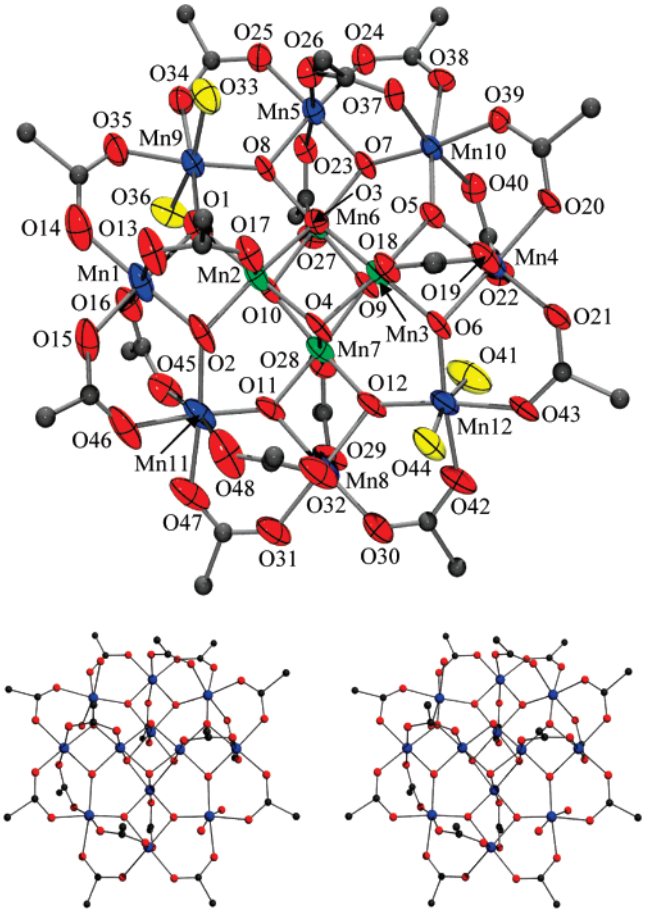

Figure 2. ORTEP representation in the PovRay format of complex **2** at the 50% probability level (except for C atoms), together with a stereopair. For clarity, only the *ipso*-C atoms of the carboxylate groups are shown. Mn^{IV}, green; Mn^{III}, blue; O, red; H_2O, yellow; C, gray.

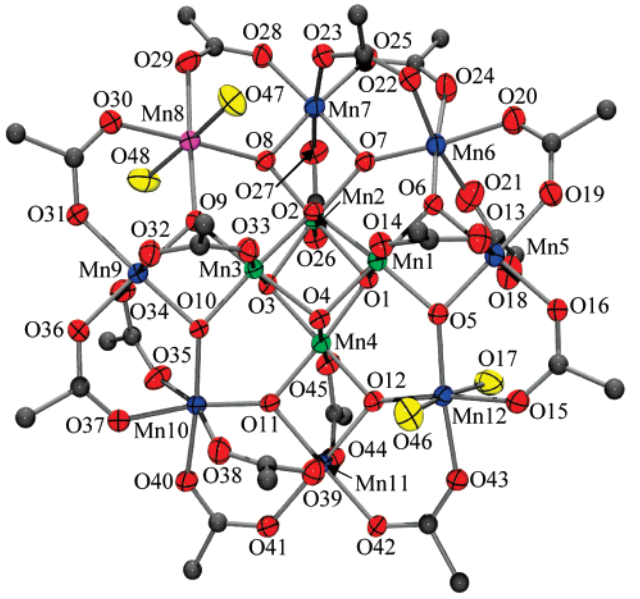

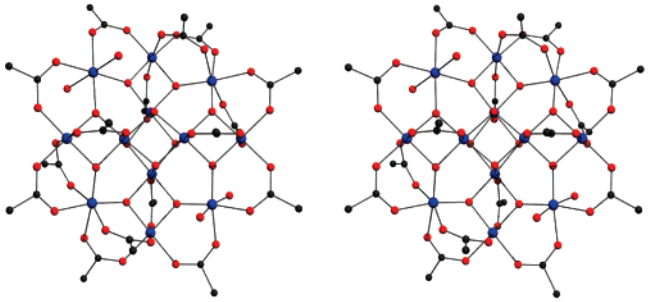

Figure 3. ORTEP representation in the PovRay format of the anion of complex **3** at the 50% probability level (except for C atoms), together with a stereopair. For clarity, only the *ipso*-C atoms of the carboxylate groups are shown. Mn^{IV}, green; Mn^{III}, blue; Mn^{II}, purple; O, red; H_2O, yellow; C, gray.

$(O_2CPh)_{16}(H_2O)_4]$, $[Mn_{12}O_{12}(O_2CC_6H_4$-*p*-$Cl)_{16}(H_2O)_4]$, $[Mn_{12}O_{12}(O_2CMe)_8(O_3SPh)_8(H_2O)_4]$, and others.[9b,23h,35]

All of the Mn centers are six-coordinate with near-octahedral geometry. Assignment of the oxidation states of the metal centers was done qualitatively by charge consideration and also by comparison of the bond distances around the Mn centers. These assignments were confirmed quantitatively by bond valence sum (BVS) calculations,[36] indicating that Mn(2), Mn(3), Mn(6), and Mn(7) are Mn^{IV}, while the remaining Mn centers are Mn^{III} (see Supporting Information). The structure of **2** is very similar to other previously characterized neutral Mn_{12} complexes. The eight Mn^{III} centers exhibit a Jahn−Teller (JT) distortion, as expected for a high-spin d^4 ion in near-octahedral geometry. As is almost always the case for Mn^{III} ions, the JT distortion takes the form of an axial elongation of two trans bonds, typically lengthening bond distances by 0.1−0.2 Å. The JT elongation axes avoid the $Mn-O^{2-}$ bonds, the shortest and strongest in the molecule, and thus the JT axes are all axially disposed, roughly perpendicular to the $[Mn_{12}O_{12}]$ disklike core. As a result, there is a near parallel alignment of the eight Mn^{III} JT elongation axes. This is also the origin of the significant magnetic anisotropy in the *z* direction that greatly influences the observed magnetic properties (vide infra).

The JT elongation axis of Mn(11) is not clearly defined, however. The axial bonds, Mn(11)−O(45) = 2.015(8) Å and Mn(11)−O(48) = 2.010(9) Å, are slightly shorter than is typical for an axially elongated JT bond of a Mn^{III} ion. In addition, the equatorial bonds, Mn(11)−O(47) = 2.053(10) Å and Mn(11)−O(2) = 1.978(8) Å, are slightly longer than is typical for a $Mn^{III}-O_{eq}$ and $Mn^{III}-O^{2-}$ bond, respectively, in a Mn_{12} complex. These abnormal distances around Mn(11) suggest a static disorder between a normal axially disposed JT elongation axis and one abnormally oriented in the plane of the molecule. We have previously called such molecules (differing only in the orientation of one or more JT axes) Jahn−Teller isomers.[37−39] Exam-

(35) Ruiz, D.; Sun, Z.; Aubin, S. M. J.; Rumberger, E.; Incarvito, C.; Folting, K.; Rheingold, A. L.; Christou, G.; Hendrickson, D. N. *Mol. Cryst. Liq. Cryst.* **1999**, *335*, 413.
(36) (a) Brown, I. D.; Wu, K. K. *Acta Crystallogr.* **1976**, *B32*, 1957. (b) Palenik, G. J. *Inorg. Chem.* **1997**, *36*, 4888.
(37) (a) Sun, Z.; Ruiz, D.; Dilley, N. R.; Soler, M.; Ribas, J.; Folting, K.; Maple, M. B.; Christou, G.; Hendrickson, D. N. *Chem. Commun.* **1999**, *19*, 1973. (b) Aubin, S. M. J.; Sun, Z.; Eppley, H. J.; Rumberger, E. M.; Guzei, I. A.; Folting, K.; Gantzel, P. K.; Rheingold, A. L.; Christou, G.; Hendrickson, D. N. *Inorg. Chem.* **2001**, *40*, 2127. (c) Aubin, S. M. J.; Sun, Z.; Eppley, H. J.; Rumberger, E. M.; Guzei, I. A.; Folting, P. K.; Gantzel, P. K.; Rheingold, A. L.; Christou, G.; Hendrickson, D. N. *Polyhedron* **2001**, *20*, 1139.
(38) Soler, M.; Wernsdorfer, W.; Sun, Z.; Huffman, J. C.; Hendrickson, D. N. Christou, G. *Chem. Commun.* **2003**, *21*, 2672.

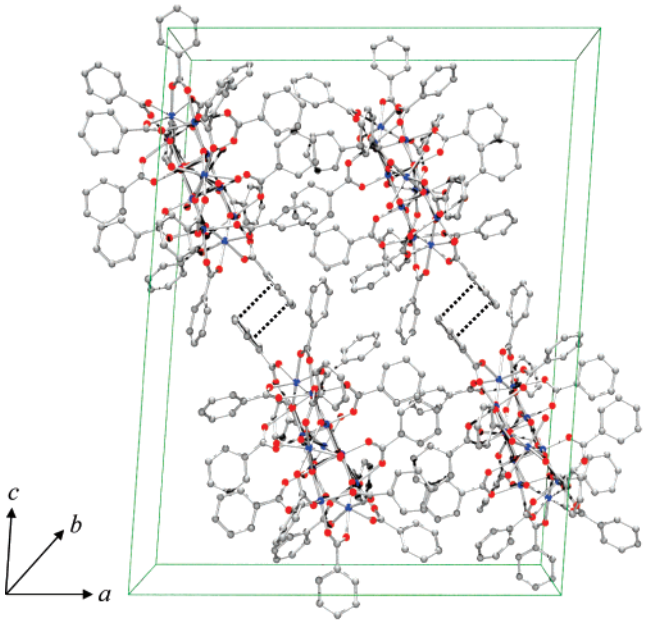

Figure 4. Packing diagram for **3** emphasizing the intermolecular π stacking of the carboxylate aromatic rings (dashed lines).

ples include $[Mn_{12}O_{12}(O_2CCH_2Bu^t)_{16}(H_2O)_4]$,[37] $[Mn_{12}O_{12}(O_2CC_6H_4$-*p*-$Me)_{16}(H_2O)_4]$,[38] and $[Mn_{12}O_{12}(O_2CCF_3)_{16}(H_2O)_4]$.[39]

Complex **3**·$4.5CH_2Cl_2$·$^1/_2H_2O$ crystallizes in the monoclinic space group *P*2/*c*. The anion again consists of a central $[Mn^{IV}_4O_4]$ cubane surrounded by a nonplanar ring of eight Mn atoms bridged by eight μ_3-O^{2-} ions, sixteen bridging $C_6F_5CO_2^-$ ligands, and four terminal H_2O molecules (Figure 3). Examination of the Mn−O bond lengths unequivocally establishes that the added electron has converted a formerly Mn^{III} atom to a Mn^{II} ion [Mn(8)]. JT axial elongations are observed at the other seven ring Mn atoms, as expected for a high-spin d^4 ion in near-octahedral geometry. All of the JT elongation axes are approximately perpendicular to the plane of the molecule. The Mn oxidation levels were determined by a BVS[36] calculation (see Supporting Information). Therefore, the $[Mn_{12}]^-$ anion is a trapped-valence Mn^{II}, Mn_7^{III}, Mn_4^{IV} cluster.

A static disorder between one carboxylate group and an adjacent water molecule is observed in the crystal structure of **3**. Hence, the structure is a mixture of two isomers, the 2:2 form (77%) and the 1:1:2 form (23%); the notation describes the distribution of the four H_2O molecules among the Mn ions. Figure 3 shows the form with 77% occupancy, where the carboxylate is bridging Mn(6) and Mn(5) [O(21)−C(64)−O(18)] and the water molecule [O(17)] is coordinated to Mn(12). The minor form has the carboxylate bridging Mn(12) and Mn(5) [O(17)−C(57)−O(18)] and the water molecule [O(21)] coordinated to Mn(6).

The $[Mn_{12}]^-$ molecules are stacked in columns with all of the molecules oriented in the same way with respect to the cell axes. There is a π-stacking interaction of the pentafluorophenyl rings bridging Mn(5) and Mn(6) between

(39) Zhao, H.; Berlinguette, C. P.; Basca, J.; Prosvirin, A. V.; Bera, J. K.; Tichy, S. E.; Schelter, E. J.; Dunbar, K. R. *Inorg. Chem.* **2004**, *43*, 1359.

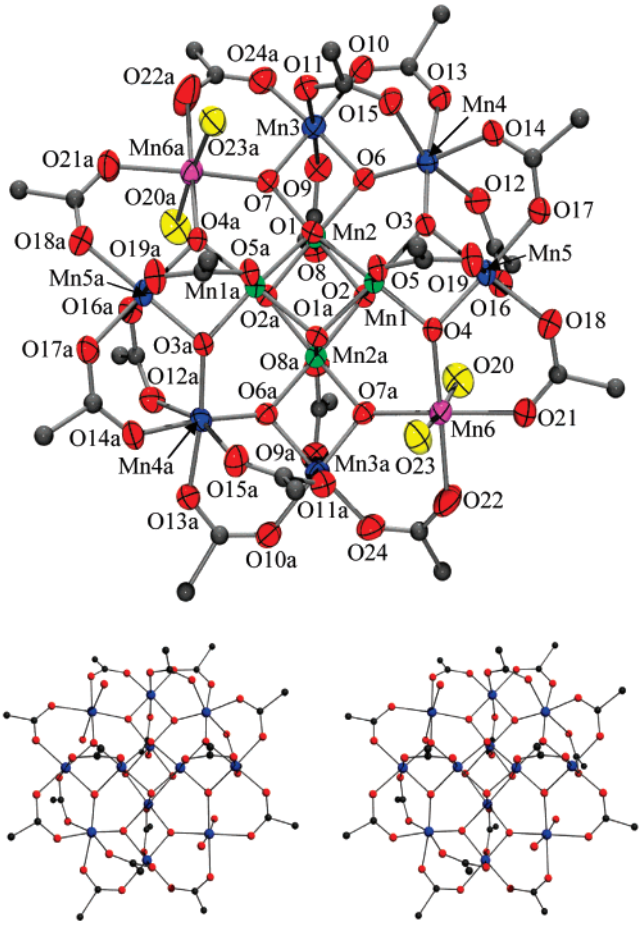

Figure 5. ORTEP representation in the PovRay format of the anion of complex **4** at the 50% probability level (except for C atoms), together with a stereopair. For clarity, only the *ipso*-C atoms of the carboxylate groups are shown. Mn^{IV}, green; Mn^{III}, blue; Mn^{II}, purple; O, red; H_2O, yellow; C, gray.

$[Mn_{12}]^-$ anions in adjacent columns along the $\bar{1}01$ direction of the cell as shown in Figure 4 as dashed lines. The dihedral angle between the rings is 1° and the ring separation is ∼3.5 Å.

Complex **4**·$6C_7H_8$ crystallizes in the monoclinic space group *C*2/*c* (Figure 5). The $[Mn_{12}]^{2-}$ cluster is located on a crystallographic C_2 rotation axis perpendicular to the plane of the molecule and passing through the central cubane unit. The anion again consists of a central $[Mn^{IV}_4O_4]$ cubane surrounded by a nonplanar ring of eight Mn atoms bridged by eight μ_3-O^{2-} ions, sixteen bridging $C_6F_5CO_2^-$ ligands, and four terminal H_2O molecules, which are bound in a 2:2 fashion to two trans Mn atoms, Mn(6) and Mn(6a).

Analysis of the Mn−O bond lengths again establishes that the central cubane Mn atoms are Mn^{IV} ions and that the added electrons have gone one each on two formerly Mn^{III} atoms converting them to Mn^{II} ions [Mn(6) and Mn(6a)], to which the water molecules are coordinated. The distances around Mn(6) and Mn(6a) are typical of Mn^{II} ions in near-octahedral geometry. The other six outer-ring Mn atoms display bond distances and JT axial elongations typical of Mn^{III}. All JT elongation axes are perpendicular to the plane of the molecule. The Mn oxidation levels were confirmed

Table 5. Comparison of Selected Bond Distances (Å) and Angles (deg) for Complexes **2**·3CH_2Cl_2, **3**·4.5CH_2Cl_2·$^1/_2H_2O$, and **4**·6C_7H_8

parameter[a]	**2**	**3**	**4**
$Mn^{IV}-O_c$ (ax)	1.898(6)−1.906(6)	1.874(3)−1.915(3)	1.889(3)−1.893(3)
$Mn^{IV}-O_c$ (eq)	1.895(7)−1.927(6)	1.905(3)−1.967(3)	1.921(4)−1.945(4)
$Mn^{IV}-O_r$	1.850(7)−1.894(6)	1.818(3)−1.903(3)	1.830(4)−1.877(4)
$Mn^{IV}-O_{ax}$	1.914(7)−1.931(6)	1.924(3)−1.951(3)	1.940(4)−1.947(3)
$Mn^{IIIb}-O_r$	1.874(7)−1.915(7)	1.842(3)−1.919(3)	1.841(4)−1.904(4)
$Mn^{IIIc}-O_r$	1.865(6)−1.903(6)	1.860(3)−1.915(3)	1.878(4)−1.882(4)
$Mn^{IIIb}-O_{eq}$	1.909(8)−1.960(6)	1.919(3)−1.981(3)	1.944(5)−1.980(4)
$Mn^{IIIc}-O_{eq}$	1.956(6)−1.978(7)	1.947(3)−2.031(4)	1.967(4)−1.979(4)
$Mn^{IIIb}-O_{ax}$	2.161(7)−2.244(10)	2.164(3)−2.236(4)	2.171(4)−2.268(4)
$Mn^{IIIc}-O_{ax}$	2.148(7)−2.162(8)	2.069(4)−2.163(3)	2.151(4)−2.180(4)
$Mn^{IIIc}-O_w$	2.168(7)−2.212(7)	2.207(4)−2.221(4)	−
$Mn^{IId}-O_r$	−	2.080(3)−2.153(3)	2.075(4)−2.117(4)
$Mn^{IId}-O_{eq}$	−	2.135(3)−2.164(3)	2.126(5)−2.139(5)
$Mn^{IId}-O_w$	−	2.179(4)−2.200(4)	2.219(4)−2.281(4)
$O_r-Mn^{IV}-O_r$	83.9(3)−84.8(3)	83.36(13)−84.46(13)	84.07(16)−84.26(16)
$O_r-Mn^{IIIb}-O_r$	82.3(3)−83.4(3)	82.53(13)−83.91(13)	82.49(15)−83.09(16)
$O_r-Mn^{IIIc}-O_r$	91.7(3)−95.1(3)	93.64(13)−95.31(13)	93.88(15)
$O_r-Mn^{IId}-O_r$	−	88.63(12)	93.37(14)

[a] O_c = cubane O^{2-}, O_r = ring O^{2-}, O_{ax} = axial carboxylate, O_{eq} = equatorial carboxylate, O_w = water. [b] Mn^{IIIb} atoms: Mn(1, 4, 5, and 8) in **2**, Mn(5, 7, 9, and 11) in **3**, and Mn(3 and 5) in **4**. [c] Mn^{IIIc} atoms: Mn(9, 10, 11, and 12) in **2**, Mn(6, 10, and 12) in **3**, and Mn(4) in **4**. [d] Mn^{II} atoms: Mn(8) in **3**, and Mn(6) in **4**. Distances around Mn(11) in complex **2** are not included because of disorder in the structure.

by a BVS[36] calculation (see Supporting Information). Thus, the $[Mn_{12}]^{2-}$ anion is a trapped-valence Mn_2^{II}, Mn_6^{III}, Mn_4^{IV} species.

Table 5 shows a comparison of the average Mn−O bond distances for the three $[Mn_{12}O_{12}(O_2CC_6F_5)_{16}(H_2O)_4]^z$ [$z = 0$ (**2**), 1− (**3**), and 2− (**4**)] complexes. This comparison confirms that the bond distances in the $[Mn_{12}O_{12}]$ cores are almost superimposable except for those positions that involve Mn^{II} ions being compared with Mn^{III} ions.

^{19}F NMR Spectroscopy. A ^{19}F NMR spectroscopic investigation of complexes **2**, **3**, and **4** in CD_2Cl_2 was carried out to assess the structures and stability of the complexes in solution. Chemical shifts and T_1 times for **2**−**4** are listed in Table 6. ^{1}H NMR spectroscopy has proven in the past to be a convenient tool for the study of Mn_{12} complexes, and the use of ^{19}F NMR spectroscopy in the present work is a useful complement, providing a rare example of this type of NMR spectroscopy on a paramagnetic system. The ^{19}F NMR spectrum of complex **2** in CD_2Cl_2 in Figure 6 (bottom) shows eight resonances with a 4:2:2:1:2:1:2:4 integration ratio. As with other Mn_{12} derivatives, there are only three distinct types of bridging carboxylates in the NMR spectrum: (i) four axial ligands bridging the $Mn^{III}\cdots Mn^{IV}$ pairs, (ii) four axial ligands bridging the $Mn^{III}\cdots Mn^{III}$ pairs, and (iii) eight equatorial ligands bridging the $Mn^{III}\cdots Mn^{III}$ pairs. Solution studies of Mn_{12} molecules at room temperature have shown that there is a fluxional process that is fast on the NMR time scale which rapidly exchanges the water ligands with one type of axial carboxylate ligand;[23f] the one that has both of its O atoms located on the JT elongation axes of the $Mn^{III}\cdots Mn^{III}$ pairs. This introduces dihedral mirror planes, which make all of the equatorial carboxylate groups equivalent. In effect, the solution-state symmetry of a Mn_{12} molecule is D_{2d}, giving three resonances in a 1:1:2 relative integration ratio (axial/axial/equatorial). Hence, **2** should exhibit three resonances

Table 6. Solution ^{19}F NMR Spectral Data for $[Mn_{12}O_{12}(O_2CC_6F_5)_{16}(H_2O)_4]^{0,1-,2-}$ Complexes

	peak[a]	assignment[b]	T_1[c]
2	−77.8	*o* eq (III−III)	2.8
	−114.4	*o* ax (III−IV)	3.4
	−133.7	*p* eq (III−III)	35.5
	−138.2	*p* ax (III−III)	22.5
	−142.2	*m* ax (III−III)	11.2
	−147.1	*p* ax (III−IV)	24.8
	−152.9	*m* ax (III−IV)	15.0
	−167.6	*m* eq (III−III)	19.0
3	−86.6	*o* eq (III−III)	2.4
	−109.8	*o* ax (III−IV)	3.4
	−138.8	*p* eq (III−III)	30.2
	−139.7	*p* ax (III−III)	19.3
	−140.3	*m* ax (III−III)	9.3
	−149.6	*p* ax (III−IV)	22.3
	−153.4	*m* ax (III−IV)	12.8
	−163.5	*m* eq (III−III)	15.1
4	−98.2	*o* eq (III−III)	2.2
	−115.3	*o* ax (III−IV)	3.3
	−139.3	*m* ax (III−III)	7.5
	−143.3	*p* ax (III−III)	16.6
	−145.1	*p* eq (III−III)	24.8
	−153.0	*p* ax (III−IV)	19.3
	−154.0	*m* ax (III−IV)	11.5
	−158.4	*m* eq (III−III)	13.1

[a] In ppm at ∼23 °C. [b] ax = axial, eq = equatorial; III−III and III−IV refer to ligands bridging $Mn^{III}Mn^{III}$ and $Mn^{III}Mn^{IV}$ pairs, respectively; *o* = ortho, *m* = meta and *p* = para. [c] In ms.

each for the ortho, meta, and para positions of the three types of ligands, giving a total of nine signals. Only eight are observed however; the ortho resonance of the axial ligands bridging $Mn^{III}\cdots Mn^{III}$ pairs cannot be clearly located, and we have concluded that it is probably too paramagnetically broadened to be observed. The resonances in the ^{19}F NMR spectra of **2**−**4** are shown in Figure 6. The spectra are all very similar, exhibiting eight signals each with only minor shifts of the resonances.

Spin−lattice relaxation time (T_1) measurements were performed to aid in the assignment of the peaks. Unpaired electrons on metal centers relax at very fast rates, providing efficient pathways for nuclear relaxation; in general, the longitudinal relaxation time is directly related to the distance of a nucleus from a paramagnetic center.[40,41] Resonances were also assigned on the basis of relative integration ratios, peak broadness (r^{-6} dependence, where r is the distance to the paramagnetic centers), and comparisons with Mn_{12} derivatives possessing other carboxylate groups.[22,24] For each of the three complexes, the T_1 times can be separated into three distinct groups: two resonances with very short T_1 times, three with intermediate T_1 times, and three with long T_1 times. The resonances with the shortest times were assigned to the *o*-F nuclei; these are the resonances that are broadened and shifted the most. The resonances with the longest T_1 times were assigned to the *p*-F nuclei, while those with the intermediate T_1 times were assigned to the *m*-F nuclei.

(40) Drago, R. S. *Physical Methods for Chemists*; 2nd ed.; Saunders College: New York, 1992; pp 500−556.
(41) *NMR of Paramagnetic Molecules: Principles and Applications*; La Mar, G. N., Horrocks, W. DeW., Jr., Holm, R. H., Eds.; Academic Press: New York, 1973.

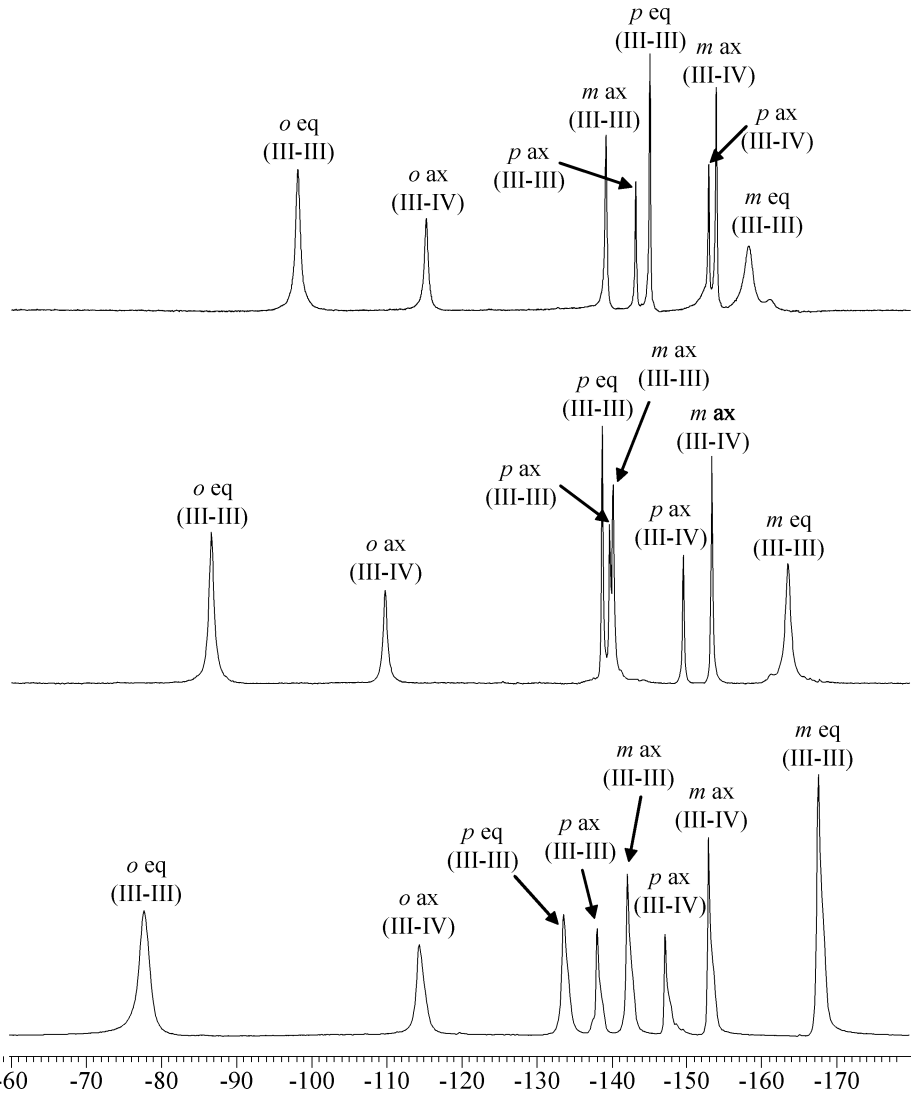

Figure 6. ^{19}F NMR (282 MHz) spectra at ~23 °C in a CD_2Cl_2 solution of **2** (bottom), **3** (middle), and **4** (top).

The paramagnetic shifts are expected to have both contact (through-bond) and dipolar (through-space) contributions.[40−42] Unpaired spin density on the paramagnetic metal centers is primarily in d_π orbitals, and π-symmetry overlap with the carboxylate π system will result in direct delocalization of positive spin density from the metal onto the $-CO_2$ π system. Direct π delocalization of the positive spin density onto the ortho and para positions of the aromatic pentafluorophenyl rings then occurs. This results in direct π delocalization of the positive spin density from the aromatic ring to the *o*- and *p*-F nuclei, giving downfield paramagnetic shifts of these NMR resonances. Spin polarization effects give a negative spin density at the meta positions of the pentafluorophenyl rings, giving an upfield paramagnetic shift of these resonances. Indeed, the observed alternating downfield−upfield−downfield shifts of the ortho, meta, and para resonances in **2**−**4** are characteristic of a dominant π-spin delocalization mechanism for the contact shifts.[41,43] The isotropic shifts from the dipolar contributions are also likely to affect the paramagnetic shifts of the fluorine nuclei in these magnetically anisotropic molecules and are probably the reason for the difference in the magnitude of the shifts of the ortho and para resonances of a particular carboxylate group, which are usually much more similar on the basis of only a π-delocalization mechanism.[41,42]

If the added electron(s) in **3** and **4** is (are) trapped on the NMR time scale, then unique resonances for the carboxylates coordinated to the Mn^{II} site(s) should be observed. This is not seen. Instead, **3** and **4** display the same D_{2d} solution symmetry as **2**, indicating that the added electrons are detrapping at a fast rate versus the ^{19}F NMR time scale among the outer ring of Mn ions.

Magnetochemistry

DC Magnetic Susceptibility Studies. Variable-temperature DC susceptibility measurements were performed on powdered microcrystalline samples of **2**, **3**, and **4**·2.5C_7H_8, restrained in eicosane to prevent torquing, in a 5.0 kG field in the temperature range of 5.0−300 K. The $\chi_M T$ versus T dependences of complexes **2** and **4**·2.5C_7H_8 are similar to those of previously studied $[Mn_{12}O_{12}(O_2CR)_{16}(H_2O)_4]$ complexes with $S = 10$ ground states, exhibiting a nearly

(42) Drago, R. S.; Zink, J. I.; Perry, W. D. *J. Chem. Educ.* **1974**, *51*, 464.

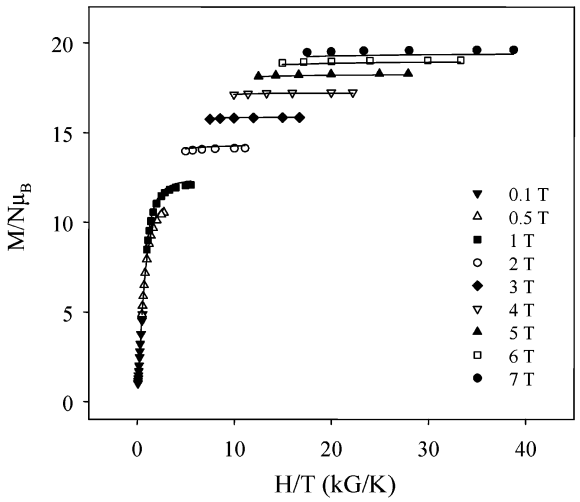

Figure 7. $M/N\mu_B$ vs H/T plot for complex **4**·2.5C_7H_8 at the indicated applied fields. The solid lines are the fit of the data; see Table 7 for the fit parameters.

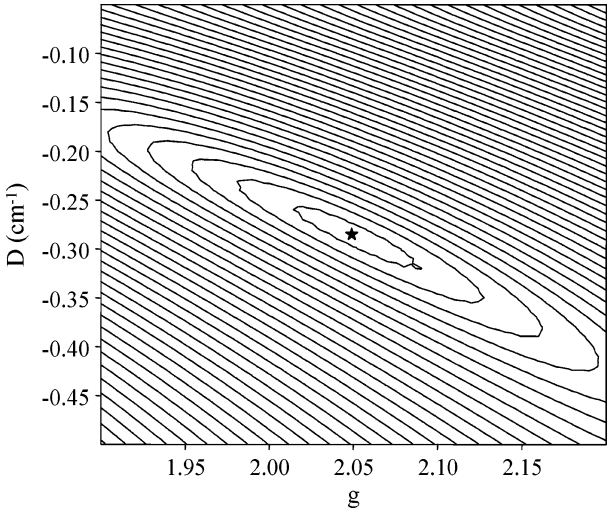

Figure 8. Two-dimensional contour plot of the error surface for the D vs g fit for complex **4**·2.5C_7H_8. The asterisk indicates the soft minimum.

Table 7. Magnetization Fit Parameters for Dried $[Mn_{12}]^z$ ($z = 0, 1-, 2-$) Complexes

	$[Mn_{12}]$ (**2**)	$[Mn_{12}]^-$ (**3**)	$[Mn_{12}]^{2-}$ (**4**)
S	10	19/2	10
g	1.87	2.04	2.05
D (cm^{-1})	−0.40	−0.34	−0.29
D (K)	−0.58	−0.49	−0.42
D/g (cm^{-1})	0.21	0.17	0.14
U (K)	58	44	42

temperature-independent value of 17−19 cm^3 K mol^{-1} (**2**) and 18−20 cm^3 K mol^{-1} (**4**·2.5C_7H_8) in the 150−300 K range which then increases rapidly to a maximum of 47−49 cm^3 K mol^{-1} (**2**) and 49−53 cm^3 K mol^{-1} (**4**·2.5C_7H_8) at ∼15 K before decreasing rapidly at lower temperatures.[2a,24] The data for the $[Mn_{12}]^-$ complex **3** show a similar temperature dependence. The $\chi_M T$ value of **3** slowly increases from 19.65 cm^3 K mol^{-1} at 300 K to a maximum of 51.35 cm^3 K mol^{-1} at 15.0 K and then decreases rapidly at lower temperatures. The maximum value indicates a high ground-state spin (S) value for each of the complexes, with the low temperature decrease primarily caused by a combination of Zeeman and zero-field splitting effects. The spin-only ($g = 2$) values for units composed of noninteracting $Mn^{IV}_4Mn^{III}_8$ (**2**), $Mn^{IV}_4Mn^{III}_7Mn^{II}$ (**3**), and $Mn^{IV}_4Mn^{III}_6Mn^{II}_2$ (**4**) ions are 31.5, 32.9, and 34.3 cm^3 K mol^{-1}, respectively. The $\chi_M T$ value of each of the complexes at 300 K is less than that expected for noninteracting metal ions, indicating the presence of appreciable intramolecular exchange interactions.

As with other Mn_{12} clusters, a theoretical treatment of the DC magnetic susceptibility data[44] as a means of determining the magnitude of the exchange parameters between the Mn ions is not simple. Instead, we concentrated only on determining the ground-state spin of the molecules using magnetization measurements in the 1−70 kG and 1.80−10.0 K ranges. The data, plotted as reduced magnetization ($M/N\mu_B$) vs H/T, are shown for representative complex **4**·2.5C_7H_8 in Figure 7, where N is Avogadro's number and μ_B is the Bohr magneton. Similar results were obtained for **2** and **3** (see Supporting Information). For a system occupying only the ground state and experiencing no zero-field splitting (ZFS), the various isofield lines would be superimposed and $M/N\mu_B$ would saturate at a value of gS. The nonsuperimposition of the isofield lines clearly indicates the presence of ZFS. The data were fit using MAGNET,[45] which assumes only the ground state is populated at these temperatures and is based on the method described elsewhere involving diagonalization of the spin Hamiltonian matrix, including axial ZFS ($D\hat{S}_z^2$) and Zeeman interactions, and incorporating a full powder average.[46] The best fits are shown as solid lines in Figure 7 for complex **4**, and the fitting parameters for complexes **2**−**4** are listed in Table 7. Attempts to fit the data with $S = 17/2$ (**3**) or $S = 9$ (**4**) gave unreasonable g values of 2.26 and 2.28, respectively; a g value significantly greater than 2 is not expected for a $Mn^{IV}_4Mn^{III}_6Mn^{II}$ or $Mn^{IV}_4Mn^{III}_6Mn^{II}_2$ cluster, and these possibilities were therefore discounted. Reasonable (but not as good) fits for **3** and **4** can also be obtained with other S values; however, the data for **3** can be fit with $S = 21/2$, $g = 2.01$, and $D = -0.32$ cm^{-1} and that for **4** with $S = 11$, $g = 1.87$, and $D = -0.24$ cm^{-1}. Nevertheless, note that the $S = 10$ (**2**), $S = 19/2$ (**3**), and $S = 10$ (**4**) ground-state values obtained from the best fits of the magnetization data are in agreement with these same values obtained from INS measurements on dried microcrystalline deuterated analogues of **2**−**4**.[26]

To confirm that the obtained parameters were the true global rather than local error minima, and to assess the uncertainty in the obtained g and D values, root-mean square D vs g error surfaces for the fits were generated using the program GRID.[47] The error surface for **4** is shown in Figure

(43) Castro, S. L.; Streib, W. E.; Sun, J.-S.; Christou, G. *Inorg. Chem.* **1996**, *35*, 4462.
(44) Kambé, K. *J. Phys. Soc. Jpn.* **1950**, *5*, 48.
(45) Davidson, E. R. *MAGNET*; Indiana University: Bloomington, IN, 1999.
(46) Yoo, J.; Yamaguchi, A.; Nakano, M.; Krzystek, J.; Streib, W. E.; Brunel, L.-C.; Ishimoto, H.; Christou, G.; Hendrickson, D. N. *Inorg. Chem.* **2001**, *40*, 4604.

8 as a contour plot for the $D = -0.05$ to -0.50 cm^{-1} and $g = 1.9$ to 2.2 ranges. One very soft fitting minimum is observed indicating significant uncertainty in the fit values; the lowest indicated contour describes the region of minimum error from $D \approx -0.26$ to -0.32 cm^{-1} and $g \approx 2.01$ to 2.09, and we thus estimate uncertainties in the fit parameters of $D = -0.29 \pm 0.03$ cm^{-1} and $g = 2.05 \pm 0.04$. Similarly, the region of minimum error for **2** is $D \approx -0.33$ to -0.48 cm^{-1} and $g \approx 1.81$ to 1.93, giving fitting parameters of $D = -0.40 \pm 0.08$ cm^{-1} and $g = 1.87 \pm 0.06$, and for **3**, it is $D \approx -0.30$ to -0.39 cm^{-1} and $g \approx 1.99$ to 2.09, giving fitting parameters of $D = -0.34 \pm 0.04$ cm^{-1} and $g = 2.04 \pm 0.05$. The soft (shallow) fitting minima and the resulting large uncertainties are undoubtedly the primary reason that the *g* values are slightly greater than two in some cases; this is not expected for Mn. We did not feel it appropriate to fix *g* at 2.0, preferring to quote, in Table 7, the values given by the fit. The similarly significant uncertainties in the *D* values quoted in Table 7 mean that they are most useful for relative comparisons, and their absolute values should be treated with some caution. Also note that the *D*/*g* values obtained from the magnetization fits will be useful for comparisons with the more reliable *D*/*g* values obtained from hysteresis studies (vide infra). More reliable values of *D* have also been obtained from the INS measurements:[26] this sensitive technique detected two species present in each sample with *D* values of -0.463 and -0.437 cm^{-1} for **2**, -0.368 and -0.332 cm^{-1} for **3**, and -0.274 and -0.241 cm^{-1} for **4**, in satisfying agreement with the single values obtained from the magnetization fits given in Table 7.

A comparison of the fitting parameters shows that the ground-state spin of each of the complexes changes only slightly as the Mn_{12} molecule is progressively reduced. The spin value does not change at all on two-electron reduction, suggesting that the complexes act as "spin buffers", accepting electrons with little or no change to the *S* value.[24] This behavior is in contrast to that observed with the axial magnetic anisotropy parameter, *D*; as the Mn_{12} molecule is progressively reduced, the magnetic anisotropy decreases, as reflected in the decreasing absolute value of *D*. This trend is expected; the molecular anisotropy of a cluster is primarily a consequence of the single-ion anisotropies of the constituent metal ions and the relative orientations of the anisotropy axes of these ions with respect to each other. The primary source of the magnetic anisotropy in a Mn_{12} molecule is from the Jahn−Teller distorted Mn^{III} ions; Mn^{II} and Mn^{IV} are fairly isotropic ions. The addition of electrons to the neutral Mn_{12} molecule on reduction converts a formerly Mn^{III} ion to a Mn^{II} ion. This results in a decrease in the number of Mn^{III} ions and a concomitant decrease in the molecular anisotropy.

The combination of a large ground-state spin and a negative magnetic anisotropy that has been decreased but is still reasonably large implies that in addition to complex **2**, the reduced complexes, **3** and **4**, might still function as SMMs as has been previously found for other one- and two-electron reduced species.[22,23c,24,33] In order for these molecules to behave as SMMs, they must possess a sufficiently large energy barrier to magnetization reversal so that they display slow magnetization relaxation rates. The upper limit (*U*) of this energy barrier is given by $U = S^2|D|$ and $U = (S^2\text{-}1/4)|D|$ for integer and noninteger spins, respectively.[1−3] These values of *U* for **2**−**4** are included in Table 7. Both AC susceptibility studies and DC magnetization studies below 1.8 K using a micro-SQUID[31] apparatus were therefore performed.

AC Magnetic Susceptibility Studies. On the basis of similar measurements on other $[Mn_{12}]$, $[Mn_{12}]^{1-}$ and $[Mn_{12}]^{2-}$ systems,[24] we expected that complexes **2**−**4** would exhibit at least one frequency-dependent out-of-phase AC susceptibility signal (χ_M''), an indicator of slow magnetization relaxation. Such signals have been observed for all Mn_{12} SMMs and are considered a signature of the SMM property; although only hysteresis loops obtained from magnetization vs DC field scans provide definitive evidence of the SMM property. Key kinetic parameters can be obtained from χ_M'' vs *T* data, including U_{eff}, the true or effective barrier to relaxation: U_{eff} is smaller than *U* because quantum tunneling of the magnetization (QTM) represents a short-cut through the barrier via higher-lying M_S levels of the ground-state *S* spin manifold. In addition, the in-phase AC susceptibility (χ_M') is invaluable for the determination of the ground-state spin of a molecule.[20,21,48] In Figure 9, the $\chi_M'T$ vs *T* plots for **2**−**4** at different AC oscillation frequencies are shown: the $\chi_M'T$ values are temperature-independent down to the temperatures at which decreases caused by slow magnetization relaxation are reached. The temperature-independent $\chi_M'T$ values show that only the ground states of the molecules are populated at these temperatures and can be used to calculate the ground-state *S* values without complications from a DC field. The $\chi_M'T$ values of ∼48, ∼47, and ∼54 cm^3 K mol^{-1} for **2**, **3**, and **4**, respectively, correspond to $S = 10/g = 1.87$, $S = 19/2/g = 1.95$, and $S = 10/g = 1.98$, respectively, consistent with the fits of the DC magnetization data above.

The sharp decreases in the $\chi_M'T$ signal at the lowest temperatures are accompanied by the appearance of frequency-dependent out-of-phase (χ_M'') signals, the characteristic signature of a superparamagnet-like species, such as an SMM. These were studied in detail, for both the dried samples and those maintained in contact with their mother liquor to avoid solvent loss. Previous studies have shown that environmental factors strongly influence the magnetic behavior of a SMM. Disordered solvent molecules of crystallization, the loss of such solvent molecules, and other environmental factors such as the site-symmetry of a molecule (the crystal space group) have accounted for the following: (i) a broadening or smearing out of QTM steps in hysteresis loops so that the loops appear smooth, without the periodic steps expected for a SMM,[5g,19l,20,21] (ii) the appearance of a second peak in the out-of-phase AC susceptibility that is indicative of a second relaxation

(47) Davidson, E. R. *GRID*; Indiana University: Bloomington, IN, 1999.

(48) Sañudo, E. C.; Wernsdorfer, W.; Abboud, K. A.; Christou. G. *Inorg. Chem*. **2004**, *43*, 4137.

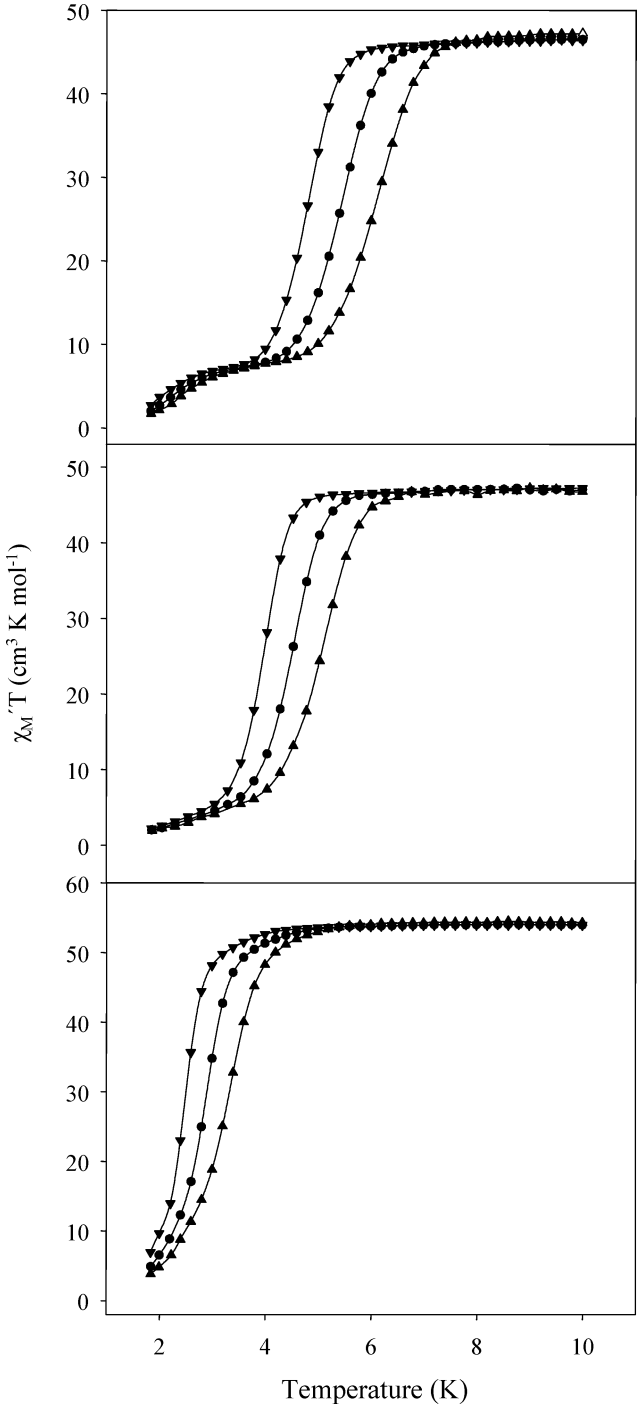

Figure 9. $\chi_M'T$ vs T plots for vacuum-dried [Mn_{12}] complexes **2** (top), [Mn_{12}]$^-$ complex **3** (middle), and [Mn_{12}]$^{2-}$ complex **4** (bottom) at 1000 (▲), 250 (●), and 50 Hz (▼).

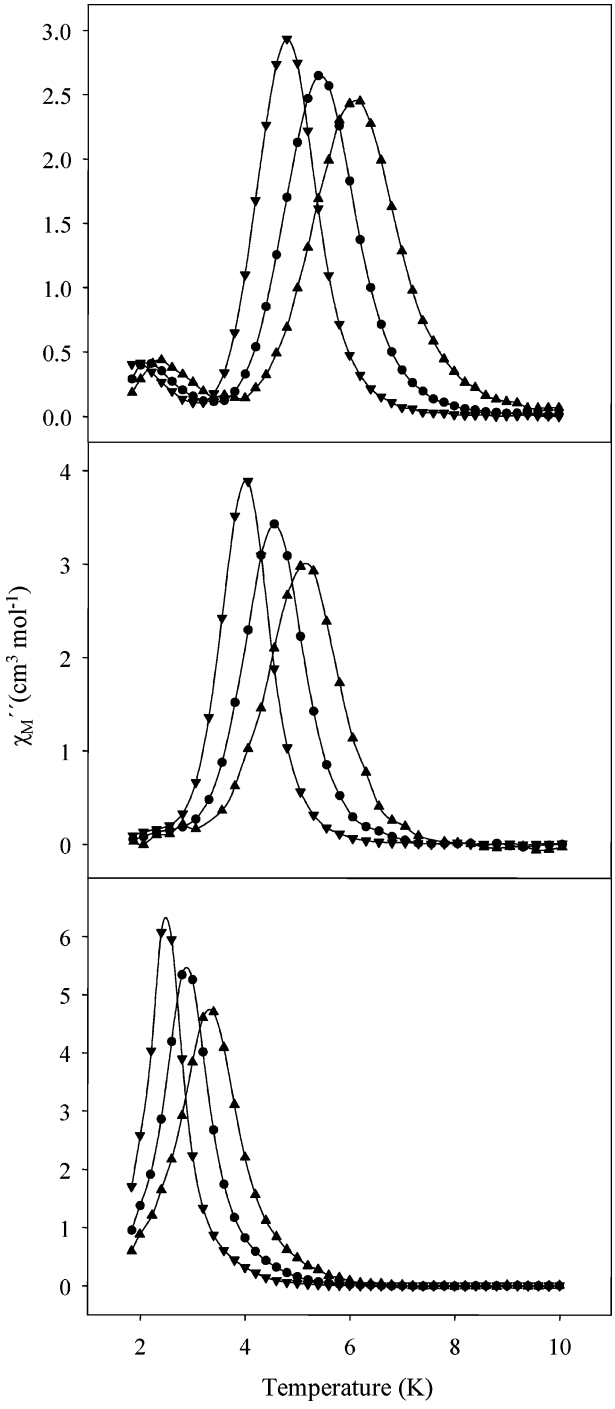

Figure 10. χ_M'' vs T plots for vacuum-dried [Mn_{12}] complexes **2** (top), [Mn_{12}]$^-$ complex **3** (middle), and [Mn_{12}]$^{2-}$ complex **4** (bottom) at 1000 (▲), 250 (●), and 50 Hz (▼).

process,[37] and (iii) differences in the effective energy barrier (U_{eff}) for magnetization reversal between seemingly identical molecules.[24] Hence, it is important to probe the relaxation behavior of SMMs by measurements on both the vacuum-dried samples and the wet samples maintained in mother liquor to prevent solvent loss. For this reason, AC susceptibilities were measured in a 3.5 G AC field oscillating at frequencies up to 1500 Hz for dried samples **2**, **3**, and **4**·2.5C_7H_8 and wet crystals of **2**·3CH_2Cl_2, **3**·4.5CH_2Cl_2·$^1/_2H_2O$, and **4**·6C_7H_8, facilitating an assessment of the effect of solvent loss on the magnetic properties.

A comparison of the χ_M'' vs T plots for the dry and wet samples of **2** at three AC oscillation frequencies is shown in the top panels of Figures 10 and 11, respectively. In each plot, two peaks corresponding to two distinct relaxation processes are shown. In the dry sample, the higher-temperature (HT) peak at ~6 K predominates with a relative integration ratio of approximately eleven times that of the lower-temperature (LT) peak at ~2.5 K, whereas in the wet sample, the HT signal predominates over the LT form by more than 30-fold. Because the integration ratio of HT/LT is much larger for the wet crystals than it is for the dry

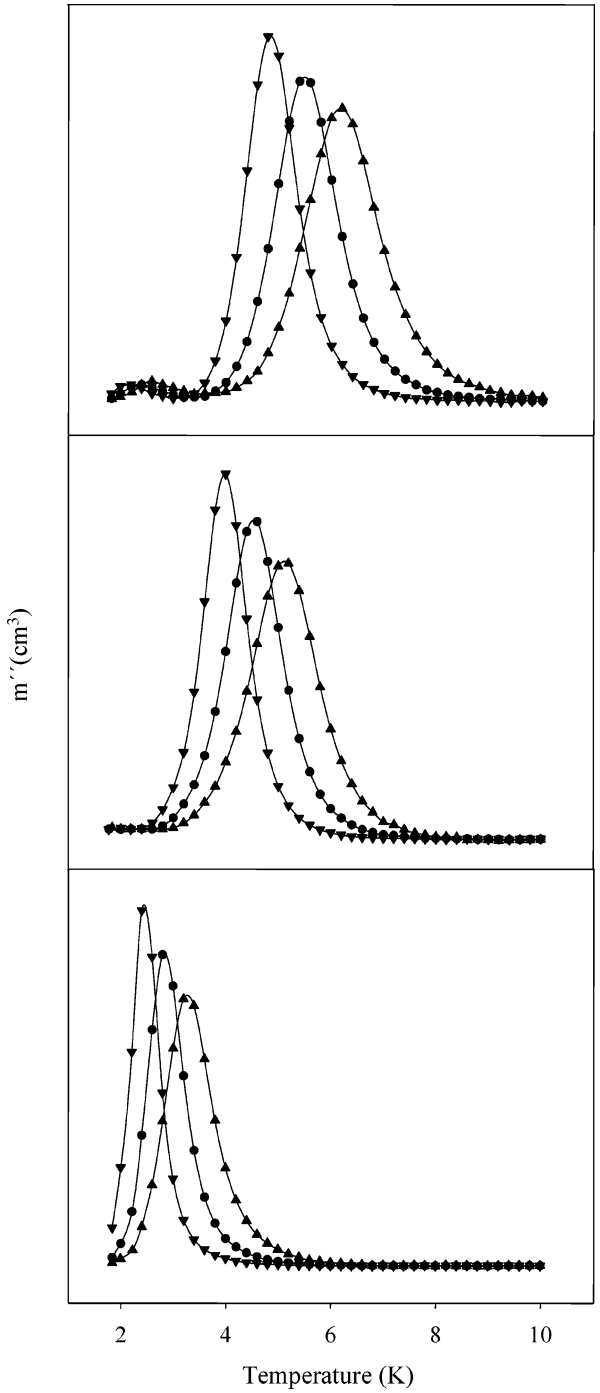

Figure 11. m'' vs T plots for wet crystals of $[Mn_{12}]$ complexes **2** (top), $[Mn_{12}]^-$ complex **3** (middle), and $[Mn_{12}]^{2-}$ complex **4** (bottom) at 1000 (▲), 250 (●), and 50 Hz (▼).

sample, it seems reasonable that the LT peak results from the loss of the highly volatile CH_2Cl_2 solvent molecules of crystallization. This solvent loss is deliberate and complete in the vacuum-dried sample, giving two molecular environments, each giving a χ_M'' signal. The presence of two χ_M'' signals is commonly encountered for Mn_{12} complexes and has been previously attributed to Jahn−Teller isomerism,[37−39] a phenomenon by which molecules differ in the relative orientation of one or more of the Mn^{III} JT elongation axes. The LT χ_M'' signal corresponds to the isomer with at least one abnormally oriented JT elongation axis toward a bridging oxide ion while the HT χ_M'' signal corresponds to the isomer with eight normally oriented JT elongation axes. Consistent with most of the previous findings, the LT form in **2** is the minor species not only in the dried microcrystalline sample but also, especially, in the wet crystals. The X-ray crystal structure of **2** reveals that the JT elongation axis of Mn(11) is not clearly defined, as already discussed, suggesting that a static disorder of the abnormally oriented JT axis of this ion might exist and that the JT elongation axis of Mn(11) might be reorienting as interstitial solvent molecules of crystallization are lost. Note that, instead of molar susceptibility, the figure ordinates for a sample maintained in the mother liquor are simply the total magnetization (plotted as $m'T$ and m'') as the mass of a wet sample cannot be accurately determined. A comparison of the U_{eff} and preexponential factor $1/\tau_0$ values in Table 8 for the HT peak of the wet and dry samples shows that the relaxation process is probably the same in each sample.

Table 8. Arrhenius Parameters (U_{eff} and τ_0) for Wet[a] and Dried[b] Complexes **2**−**4**

		τ_0 (s)	U_{eff} (K)
wet[a,c]	**2**[e]	2.9×10^{-9}	64
	3[f]	4.9×10^{-9}	53
	4[g]	3.3×10^{-8}	28
dried[b,c]	**2**[h]	3.3×10^{-9}	66
	3[h]	4.0×10^{-9}	54
	4[i]	2.7×10^{-8}	29
wet[a,d]	**2**[e]	8.1×10^{-9}	59
	3 [f,j]	3.0×10^{-10}	49
	3 [f,k]	1.3×10^{-10}	21
	4[g]	9.1×10^{-8}	25

[a] Crystals maintained in contact with the mother liquor. [b] Vacuum-dried crystals. [c] AC data only. [d] Combined AC and DC data. [e] **2**·$3CH_2Cl_2$. [f] **3**·$4.5CH_2Cl_2$·$^1/_2H_2O$. [g] **4**·$6C_7H_8$. [h] Unsolvated. [i] **4**·$2.5C_7H_8$. [j] Slower-relaxing species. [k] Faster-relaxing species.

The χ_M'' vs T plot for the dry and wet samples of both **3** and **4**·$2.5C_7H_8$ at three frequencies are shown in the middle and bottom panels of Figures 10 and 11, respectively. Only one peak is observed for each molecule at temperatures above 1.8 K, suggesting effectively only one molecular environment, a small range of axial and rhombic anisotropy parameters, D and E, and consequently a small range of U_{eff} values. For **3**, the crystal structure reveals a static disorder between a carboxylate group and an adjacent water molecule, as described earlier, giving a mixture of isomers (77:23%) differing in the distribution of the four H_2O ligands. However, only one χ_M'' peak is seen, suggesting either that (i) the two isomers have very similar D and U_{eff} values and thus relax at essentially the same rate, or (ii) the differences in the D and U_{eff} values are so large that the faster-relaxing form gives signals at <1.8 K, the operating limit of our SQUID instrument. Studies at lower temperatures are needed to address this point further (vide infra).

In accordance with the decreasing Mn^{III} content, the χ_M'' signals shift to lower temperatures on progressive reduction: 6−8 K for $[Mn_{12}]$, 4−6 K for $[Mn_{12}]^-$, and 2−4 K for $[Mn_{12}]^{2-}$. This shift reflects the decreasing energy barrier to magnetization relaxation, U_{eff}. As expected, the change in U_{eff} with decreasing Mn^{III} content is not linear. U_{eff} depends

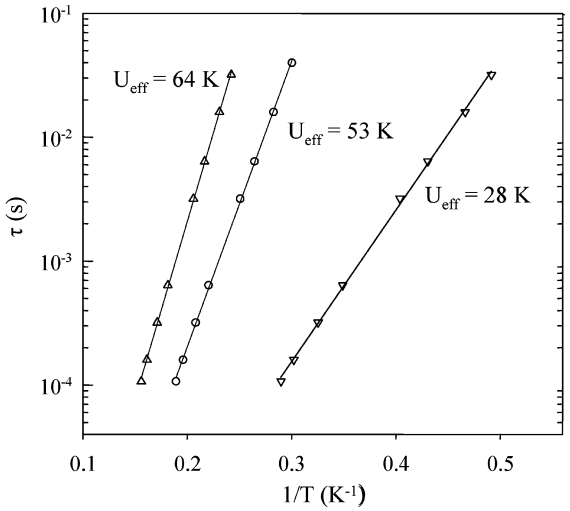

Figure 12. Plots of relaxation time (τ) vs $1/T$ for wet crystals of complexes **2** (△), **3** (○), and **4** (▽) using AC χ_M'' data. The solid lines are the fits to the Arrhenius equation. See Table 8 for the fit parameters.

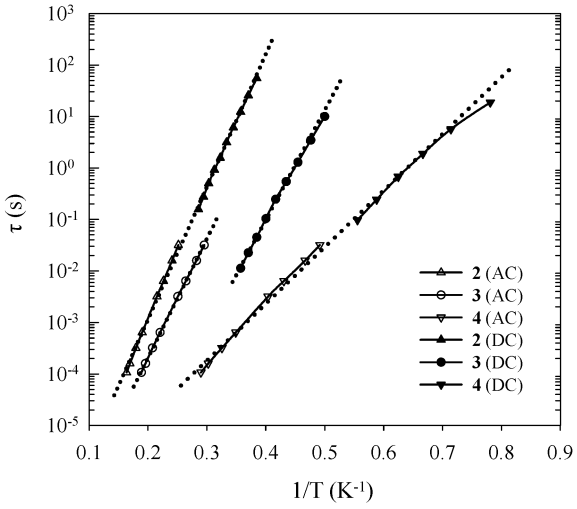

Figure 13. Plots of relaxation time (τ) vs $1/T$ for complexes **2**−**4** using AC χ_M'' and DC decay data. The dotted lines are fits to the Arrhenius equation. See Table 8 for the fit parameters.

on a number of factors, including S, the axial (D) and rhombic (E) ZFS parameters, fourth-order spin Hamiltonian parameters, and others. Qualitative comparisons, however, are reasonable and display a monotonic decrease of U_{eff} with Mn^{III} content.

Relaxation Studies Using AC and DC Data. The temperature at the peak of the χ_M'' signal is the point at which the rate of reorientation (relaxation) of the magnetization vector equals the operating frequency of the oscillating field. This is thus a source of kinetic data, and U_{eff} can be determined by fitting the resulting relaxation rate ($1/\tau$) vs T data to the Arrhenius equation (eq 3), where τ is the relaxation time.

$$\tau = \tau_0 \exp(U_{eff}/kT) \tag{3}$$

This is the characteristic behavior of a thermally activated Orbach process, where k is the Boltzmann constant and $1/\tau_0$ is the pre-exponential term. The frequency dependence of the χ_M'' peak for complexes **2**−**4** was determined at eight oscillation frequencies in the 5−1500 Hz range. Plots of τ vs $1/T$ for the wet crystals of **2**−**4** are shown in Figure 12, with the least-squares fit to eq 3 shown as a solid line. The U_{eff} and τ_0 values for both the dried microcrystalline samples and the wet crystals are compiled in Table 8 and are similar to values previously obtained for the $[Mn_{12}]$, $[Mn_{12}]^-$, and $[Mn_{12}]^{2-}$ systems. The U_{eff} and τ_0 values for wet and dried samples are almost identical, within experimental uncertainty.

Additional relaxation vs time measurements were obtained at temperatures below 1.8 K by the DC magnetization decay vs time measurements to supplement the AC data. These data were obtained on single crystals using a micro-SQUID apparatus. First, a large DC field of 1.4 T was applied to the sample at ~5 K to saturate its magnetization in one direction, and the temperature was lowered to a chosen value between 0.04 and 2 K. When the temperature was stable, the field was swept from 1.4 to 0 T at a rate of 0.14 T/s, and then the magnetization in the zero field was measured as a function of time. This gave a set of relaxation time (τ) vs T data, which were combined with the AC data and used to construct an Arrhenius plot. The data are plotted as τ vs $1/T$ in Figure 13, together with the fits (dotted lines) to eq 3; the fit parameters are given in Table 8. Good fits of the combined AC and DC data were obtained for **2** and **4**; the U_{eff} for the HT (slower-relaxing) JT isomer of **2** is 59 K, a typical value for Mn_{12}, while U_{eff} for **4** is 25 K. These can be compared with 64 and 28 K, respectively, for the wet crystals over the smaller T range of Figure 12.

There is an interesting discrepancy between the AC and DC data for **3** in Figure 13, which are U_{eff} = 53 K, $\tau_0 = 4.9 \times 10^{-9}$ s and U_{eff} = 49 K, $\tau_0 = 3.0 \times 10^{-10}$ s, respectively. Thus, the slopes of the plots (i.e., the U_{eff} values) are almost the same within experimental uncertainty, but the significant difference in τ_0 values (greater than an order of magnitude) causes a noticeable offset. Both the AC and DC measurements were repeated several times on different crystals with the same result. We are not sure of the exact origin of this difference, but it may be due to differences caused by the differing mounting conditions: the AC data were obtained on crystals, maintained in mother liquor, that were quickly transferred to the SQUID and cooled to low temperatures to avoid solvent loss, whereas the DC data were on single crystals in Apiezon grease. Crystals of **3**·$4.5CH_2Cl_2$·$^1/_2H_2O$ are very sensitive to solvent loss and readily fracture even under grease, making handling very difficult. Note that hysteresis loops described below also show greater complexity for **3**·$4.5CH_2Cl_2$·$^1/_2H_2O$ compared with those for **2**·$3CH_2Cl_2$ and **4**·$6C_7H_8$.

More detailed AC experiments were carried out on wet crystals of **2**·$3CH_2Cl_2$, **3**·$4.5CH_2Cl_2$·$^1/_2H_2O$, and **4**·$6C_7H_8$ to further the understanding of the nature of the magnetization relaxation processes in these clusters. At fixed temperatures of 4.0 K for **2**, 3.4 K for **3**, and 2.2 K for **4**, the in-phase (m') and out-of-phase (m'') components of the AC magnetic susceptibility were measured as the frequency (υ) of the oscillating AC field was varied in the range of 0.1−1500 Hz. For a single relaxation process, the m' and m'' behavior as a function of angular frequency (ω) is given by

eqs 4 and 5, respectively, while for a distribution of single relaxation processes, the m' and m'' behavior is expressed by eqs 6 and 7, respectively.

$$\chi'(\omega) = \chi_s + \frac{(\chi_T - \chi_s)}{1 + \omega^2 t^2} \quad (4)$$

$$\chi''(\omega) = \frac{(\chi_T - \chi_s)\omega\tau}{1 + \omega^2 t^2} \quad (5)$$

$$\chi'(\omega) = \chi_s + \frac{(\chi_T - \chi_s)[1 + (\omega T)^{1-\alpha}\sin(\alpha\pi/2)]}{1 + 2(\omega\tau)^{1-\alpha}\sin(\alpha\pi/2) + (\omega t)^{2(1-\alpha)}} \quad (6)$$

$$\chi''(\omega) = \chi_s + \frac{(\chi_T - \chi_s)(\omega\tau)^{1-\alpha}\cos(\alpha\pi/2)}{1 + 2(\omega\tau)^{1-\alpha}\sin(\alpha\pi/2) + (\omega t)^{2(1-\alpha)}} \quad (7)$$

where χ_s is the adiabatic susceptibility, χ_T is the isothermal susceptibility, $\omega = 2\pi\upsilon$ is the angular frequency, and τ is the magnetization relaxation time. An additional parameter, α, which takes a value between 0 and 1 and gauges the width of the distribution, is included in the expressions for a distribution of single relaxation processes. Plots of m' vs m'' (Cole−Cole or Argand plots) are shown for complexes **2**−**4** in the top, middle, and bottom panels of Figure 14, respectively. A least-squares fitting of the data to a single relaxation process is shown as a dashed line, while the fitting to a distribution of single relaxation processes is shown as a solid line; clearly, significantly improved fits are obtained for the latter. On this basis, it is concluded that in wet crystals of complexes **2**−**4** the magnetization relaxes via only a single process and that there is a distribution in this single relaxation process (i.e., a distribution of relaxation barriers). The width of the distribution is gauged by the fitting parameter, α; average values of α obtained from fitting of plots of m' vs frequency and m'' vs frequency to a distribution of single relaxation processes are 0.177 (**2**), 0.210 (**3**), and 0.126 (**4**). A complete listing of the fitting parameters is included in Supporting Information. These results are consistent with similar studies done on other Mn_{12} complexes;[19d] the main conclusion is that the samples have a distribution of energy relaxation barriers (i.e., a distribution of *D* values caused by a distribution in the local molecular environments). It should be noted that, at the temperature was which the measurement was carried out for complex **3**, only the HT (slower-relaxing) isomer was studied. Similar measurements at much lower temperatures are needed to study the LT (faster-relaxing) isomer of **3**.

Hysteresis Loops. The AC measurements suggest that complexes **2**−**4** function as SMMs, and this was confirmed by hysteresis loops obtained from magnetization vs DC field scans. These were performed on single crystals of **2**·$3CH_2Cl_2$, **3**·$4.5CH_2Cl_2$·$^1/_2H_2O$, and **4**·$6C_7H_8$ using a micro-SQUID apparatus. The applied field was aligned parallel to the easy axis (*z* axis) of the molecules using the recently reported method.[49] For all three compounds, all molecules within the crystal were oriented with their *z* axes parallel, as, for example, is evident in Figure 4 for the anion of **3**. The temperature- and scan-rate dependence hysteresis studies on **2**·$3CH_2Cl_2$ are shown in Figure 15. The coercivities clearly increase with decreasing temperature and increasing scan rate, as expected for the superparamagnet-like behavior of SMMs. The loops also clearly show the steps at periodic values of applied field because of QTM, which causes a surge

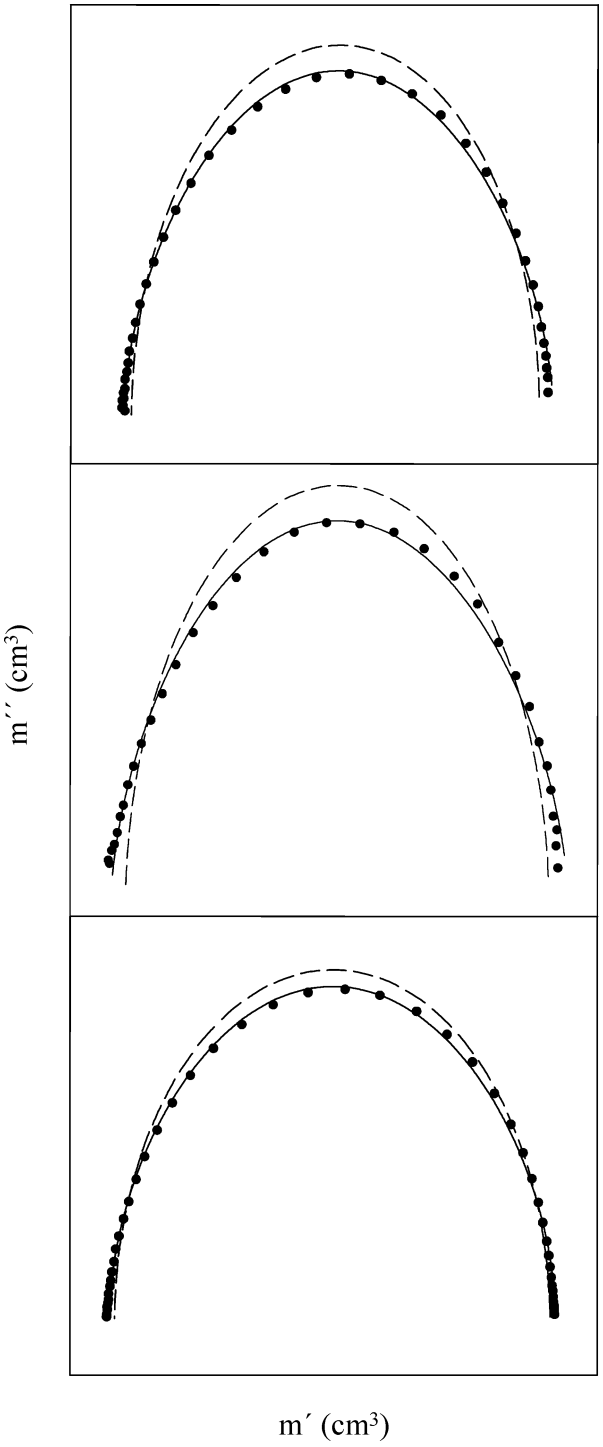

Figure 14. Argand plot of m' vs m'' for wet crystals of complex **2** at 4.0 K (top), complex **3** at 3.4 K (middle), and complex **4** at 2.2 K (bottom). The dashed line is a least-squares fitting of the data to a single relaxation process as described by eqs 5 and 6. The solid line is a least-squares fitting of the data to a distribution of single relaxation processes as described by eqs 7 and 8. See Supporting Information for the fit parameters.

(49) Wernsdorfer, W.; Chakov, N. E.; Christou, G. *Phys. Rev. B,* **2004**, *70,* 132413 (1−4).

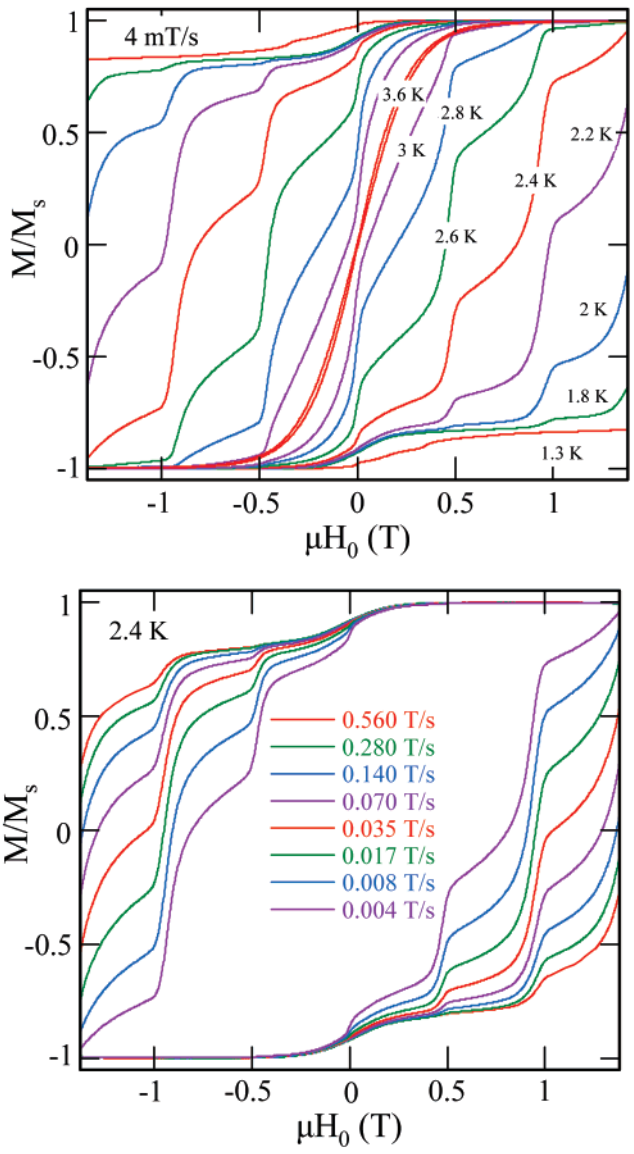

Figure 15. Magnetization hysteresis loops for a single crystal of **2**·3CH_2Cl_2: (top) the temperature dependence at a fixed scan rate of 4 mT/s, and (bottom) the scan-rate dependence at a fixed temperature of 2.4 K. *M* is normalized to its saturation value, M_s.

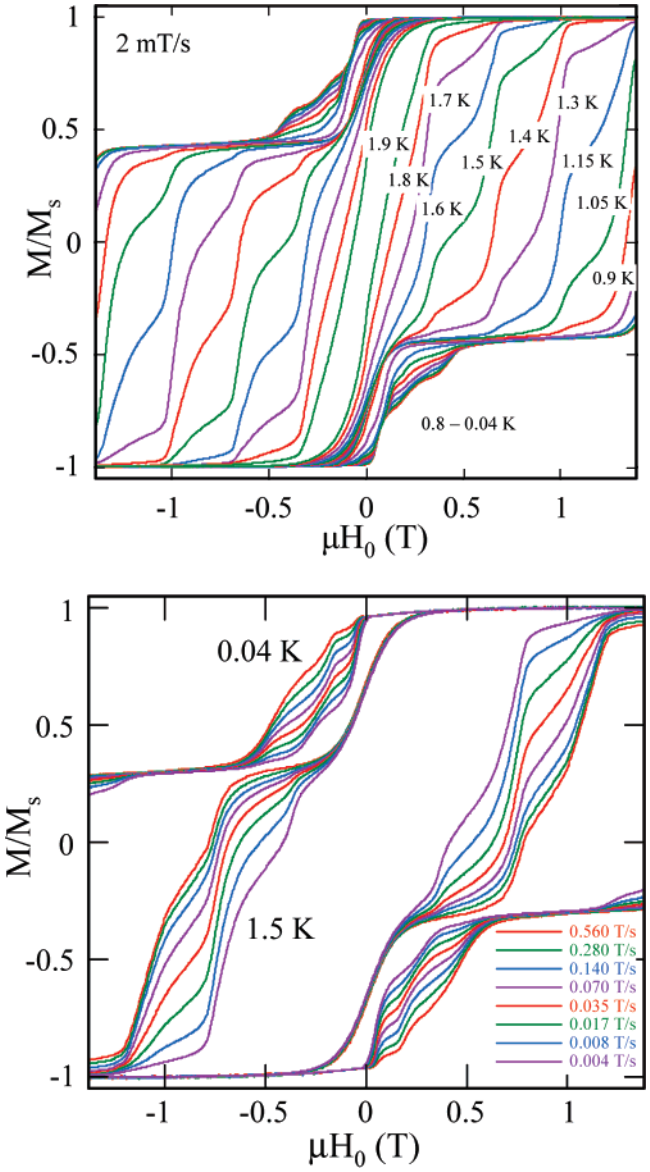

Figure 16. Magnetization hysteresis loops for a single crystal of **3**·4.5CH_2Cl_2·$^1/_2H_2O$: (top) the temperature dependence at a fixed scan rate of 2 mT/s, and (bottom) the scan-rate dependence at a fixed temperature of 0.04 K. *M* is normalized to its saturation value, M_s.

in the relaxation as the M_S levels on opposite sides of the $S = 10$ double well potential energy barrier come into resonance at those field positions. The field separation, ΔH, between the steps is proportional to *D* and is given by eq 8.

$$\Delta H = \frac{|D|}{g\mu_B} \tag{8}$$

Measurement of the step positions in Figure 15 gave an average ΔH of 0.475 T and a resulting $|D|/g$ value of 0.22 cm^{-1}, consistent with both the values obtained from fits of the magnetization data for dried **2** (0.21 cm^{-1}) and from the INS studies (0.22 cm^{-1}).[26]

The corresponding hysteresis loops on **3**·4.5CH_2Cl_2·$^1/_2H_2O$ are shown in Figure 16. They clearly reveal two different species within the crystal. Approximately 28% of the molecules have smaller U_{eff} and *D* values than the remaining 72%: analysis of the step positions of the faster-relaxing species (28%) gave an average $\Delta H \approx 0.18$ T and $|D|/g \approx 0.042$ cm^{-1}, whereas the slower-relaxing species (72%) gave $\Delta H \approx 0.33$ T and $|D|/g \approx 0.15$ cm^{-1}. The logical conclusion is that the two isomers of **3** detected in the crystal structure in a ~77:23% ratio correspond to the two species detected in the hysteresis loops of Figure 16 in a ~72:28% ratio. The much smaller *D* value of the minor component and the resulting small U_{eff} would be consistent with the AC χ_M'' signal occurring at <1.8 K and thus not being observed in Figures 10 and 11. Of course, we cannot rule out the possibility that the same ~3:1 ratio of two species in the crystal structure and the hysteresis loops may just be a coincidence and that the faster-relaxing species may in reality be the result of a JT isomer with an abnormally oriented JT axis statically disordered about multiple Mn^{III} ions and thus not showing up in the structural parameters of the X-ray structure. Finally, the examination of the loop coercivities

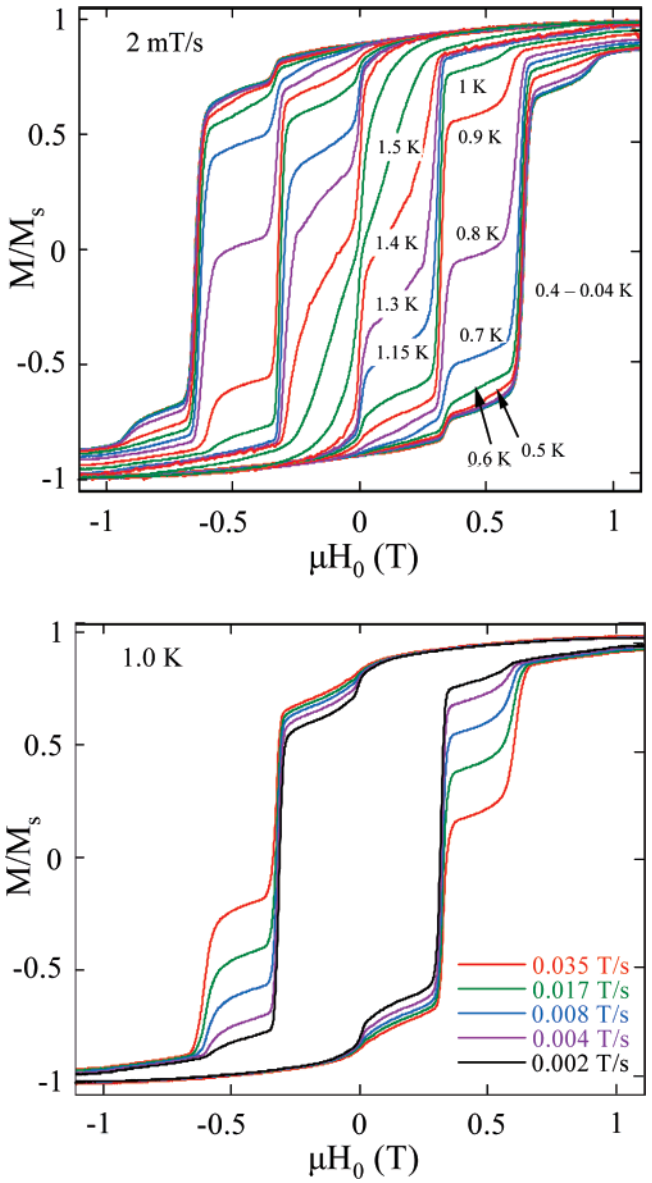

Figure 17. Magnetization hysteresis loops for a single crystal of **4**·$6C_7H_8$: (top) the temperature dependence at a fixed scan rate of 2 mT/s, and (bottom) the scan-rate dependence at a fixed temperature of 1.0 K. M is normalized to its saturation value, M_s.

for each subspecies shows that both exhibit the temperature and scan-rate dependence of a SMM. It should be noted that **3** has a half-integer spin ground state and yet shows QTM at zero applied field, apparently contradicting the prediction from the spin-parity effect that QTM should be suppressed in a half-integer system in zero applied field because of Kramer's degeneracy and only allowed in integer spin systems. In practice, however, it is impossible to ensure absolutely zero external fields, and the dipolar fields of neighboring molecules and the hyperfine fields from the ^{55}Mn nuclei ($I = 5/2$, ~ 100% natural abundance) provide a means for QTM to occur at apparently zero applied fields.

(50) Wernsdorfer, W.; Chakov, N. E.; Christou, G. *Phys. Rev. Lett.*, submitted for publication. (b) http://xxx.lanl.gov/abs/cond-mat/0503193.

Studies of this point for complexes **2**−**4** have been carried out in detail and are reported elsewhere.[50]

The corresponding hysteresis loops on **4**·$6C_7H_8$ are shown in Figure 17, and they are similar, overall, to those for **2**. There is only one species present, and the step pattern is well defined. Again, the coercivities increase with decreasing temperature and increasing scan rate, as expected for a SMM and as seen previously for another $[Mn_{12}]^{2-}$ salt.[24] Analysis of the step positions gave $|D|/g \approx 0.15$ cm^{-1}, a value consistent with those obtained from both INS[26] and magnetization vs field studies on a dried sample of this complex.

Conclusions

The goal of this investigation was to study the effect of reduction on the magnetic properties of a family of Mn_{12} SMMs with identical peripheral ligation. The syntheses, crystal structures, and magnetic properties have been obtained on such a family with pentafluorobenzoate ligands and spanning three oxidation levels. ^{19}F NMR spectra have been obtained on all three complexes, establishing retention of the structures on dissolution with fast de-trapping (on the ^{19}F NMR time scale) of the added electrons leading to effective D_{2d} solution symmetry in every case. AC and DC susceptibility studies on dried microcrystalline samples of complexes **2**−**4** establish that $S = 10$, 19/2, and 10 for **2**, **3**, and **4**, respectively, and show a decrease in the $|D|$ value with decreasing Mn^{III} content (i.e., the magnetic anisotropy decreases with reduction and thus the magnetization relaxation rate increases). Magnetization vs DC field scans exhibit hysteresis, establishing all of the compounds to be SMMs. The hysteresis loops also exhibit the steps characteristic of QTM.

AC susceptibility measurements carried out on wet crystals maintained in the mother liquor to prevent the loss of interstitial solvent and on dried microcrystalline samples showed only small differences in the values of U_{eff} and τ_0 between wet and dry samples. However, the measurements on wet crystals do avoid certain complications associated with solvent loss, such as an increase in the amount of the faster-relaxing form of **2**. This again emphasizes the importance of comparing data from different techniques using samples maintained in the same manner. For example, the data from micro-SQUID hysteresis studies on wet single crystals are best compared to magnetization studies on similarly wet crystals.

Acknowledgment. This work was supported by the National Science Foundation.

Supporting Information Available: X-ray crystallographic files in CIF format, bond valence sums and a complete listing of bond distances and angles for complexes **2**·$3CH_2Cl_2$, **3**·$4.5CH_2Cl_2$·$^1/_2H_2O$, and **4**·$6C_7H_8$, fitting parameters for plots of m' vs frequency and m'' vs frequency to a single relaxation process and a distribution of single relaxation processes, plots of $M/N\mu_B$ vs H/T for complexes **2** and **3**, plots of m' vs frequency and m'' vs frequency for complexes **2**·$3CH_2Cl_2$, **3**·$4.5CH_2Cl_2$·$^1/_2H_2O$, and **4**·$6C_7H_8$. This material is available free of charge via the Internet at http://pubs.acs.org.

IC050379W